

Document downloaded from:

<http://hdl.handle.net/10251/154994>

This paper must be cited as:

Azevedo De Carvalho, LR.; Sallica-Leva, E.; Rayón Encinas, E.; Fogagnolo, JB. (2018). Less-rigid coating in Ti obtained by laser surface alloying with Nb. *Surface and Coatings Technology*. 346:19-28. <https://doi.org/10.1016/j.surfcoat.2018.04.038>



The final publication is available at

<https://doi.org/10.1016/j.surfcoat.2018.04.038>

Copyright Elsevier

Additional Information

## Less-rigid coating in Ti obtained by laser surface alloying with Nb

Lisiane Rocha Azevedo de Carvalho <sup>a</sup>, Edwin Sallica-Leva <sup>a</sup>,  
Emilio Rayón Encinas <sup>b</sup>, João Batista Fogagnolo <sup>a,\*</sup>

<sup>a</sup> *University of Campinas, School of Mechanical Engineering, Rua Mendeleiev 200, 13083-860 Campinas, SP, Brazil*

<sup>b</sup> *Institut de Tecnologia de Materials – Universitat Politècnica de València, Camino de Vera, s/n - 46022 Valencia, Spain*

**Abstract:** The fabrication of parts with stiffness gradation specifically designed to attain higher mechanical and/or biomedical performance is receiving increasing scientific and technological interest. This work reports the use of laser surface alloying to introduce Nb into the surface layer of Ti pieces and thus obtain continuous coatings composed of Ti-Nb alloys. By controlling the laser processing parameters, coatings with lower Young's modulus and higher hardness compared to the substrate, practically free of cracks and with very low porosity were obtained, using energy densities in the range of 24 to 65 J/mm<sup>2</sup>. However, compositional heterogeneity mainly due to microsegregation during the solidification process was observed. Increasing the energy density resulted in deeper fusion zones, which increased the substrate fusion and thus decreased the Nb content and produced a coating with a microstructure predominantly composed of  $\alpha/\alpha'$  acicular phase. On the other hand, the Nb content of the coatings produced with lower energy densities was high enough ( $\sim 20\text{-}30\%$  in mass) to (meta)stabilize the less-rigid  $\alpha''$  and  $\beta$  phases, which promoted the highest reductions in the Young's modulus of the investigated coatings. Besides the lower stiffness, all coatings presented at least twice the hardness of the substrate. Maps of the properties constructed from the nanoindentation results showed that, despite the compositional heterogeneity, homogenous values of Young's modulus and hardness were attained and

the change in the interface region was gradual, in agreement with the concept of functionally graded materials.

**Keywords:** Functionally graded materials; Surface stiffness gradient; Ti-Nb alloys; Surface engineering; Instrumented indentation.

\* Corresponding author: Tel.: +55-19-35213300; fax:+55-19-32893722;  
e-mail address: fogagnolo@fem.unicamp.br (J.B. Fogagnolo).

## 1- INTRODUCTION

Functionally graded material (FGM) may be characterized by the gradual variation over volume in their physical, chemical or mechanical properties [1]. The variation in such properties along different regions of a piece or device can be very useful in many medical or engineering applications [2, 3]. Interest in FGM arose because traditional composite materials may show delamination when subjected to high thermal gradients [1, 4], due to the difference in the coefficients of thermal expansion of its composite components that are separated by sharp interfaces. Distinct kinds of FGM can be obtained through the use of a compositional gradient, porosity gradient or even microstructural gradient [2], which can be achieved during the solidification process by the application of localized thermal treatments in the solid state [5] or by localized cold mechanical deformation [6].

In nature, several examples of FGM can be observed such as teeth, bone, and bamboo [7]. The external part of the proximal femur is composed of cortical tissue, which is denser, stronger and stiffer, while the less dense trabecular tissue is present in the center [3, 7]. The synergy of such a design allows a larger bearing area with a lower weight, maximizing the mechanical performance of the femur [8]. In materials engineering, metal parts with a hardened surface and soft core are used when greater wear resistance with good toughness is required; carburized steel gears are an example of this design. As is widely known, both compositional (carbon is dissolved in the surface layers) and microstructural (quenching to form a martensitic microstructure) gradients are present in this case. Analogous to steel, titanium and its alloys can be modified superficially to obtain a hardened surface while preserving the ductility of the core. Laser surface melting (LSM), laser cladding (LC), laser surface alloying (LSA), laser surface heat treatment (LSHT) and laser shock peening (LSP) are the main

techniques that employ lasers as a heat source for surface modification [9]. The use of LSA was reported to improve the wear resistance of Ti [10-14] and Ti-6Al-4V alloy [15, 16]. A hardness increase by a factor greater than two relative to the substrate was attributed to the presence of hard ceramic phases, such as TiN [11, 12, 15], TiC [13-16] and/or TiB [14, 15]. Substitutional solid solution hardening and silicates formation [10], intermetallic precipitation [17], interstitial solid solution hardening [11] and oxide formation [12] were also reported to increase the strength of a surface layer in Ti using LSA.

In addition to the hardness gradient, pieces or devices with stiffness gradation are attracting scientific and technological interest. Previously mentioned as an example of a natural FGM, bamboo presents a stiffness gradation through its wall in which the stiffness increases from the inner to the outer surface [18]. This gradation is mainly due to the distribution of the cellulose fibers in an amorphous matrix of lignin, with the fiber/matrix ratio increasing from the inner to the outer surface. This configuration contributes to the high flexibility of bamboo. Biomedical application is currently the main field that is highlighting the usefulness of stiffness-graded materials.

Computational modeling indicated the higher mechanical performance of bone fixation plates with stiffness gradation [19]. A significant reduction of the stress in the contact of the metal femoral head with the polyethylene coating of the acetabular cup was predicted by computer simulation when using a femoral head with a less-rigid surface, that is, in which the stiffness is higher in its core and lower at its surface [20].

One approach for obtaining stiffness gradation is the insertion of a porosity gradation in the piece. Orthopedic implants with a solid core and a porous surface are desirable when better biological fixation is required because a porous surface allows the growth of bone tissue through the pores [21, 22]. Additionally, this configuration

decreases the implant weight and the effective stiffness in the bone/implant contact zone. Moreover, porosity gradation may be strategically placed in the regions where a porous implant should be joined with another functional component [23].

Another way to obtain stiffness gradation is through microstructure control. Lopes et al. [5] used a localized heat treatment to promote the precipitation of the  $\alpha$  phase in a  $\beta$  metastable matrix, promoting an increase in both the strength and Young's modulus. They proposed this processing route for the manufacture of hip implants in which a lower stiffness can be kept in the stem in order to minimize stress shielding, while a higher stiffness can be attained in the proximal region in order to lessen the undesirable micromotions that may induce growth of fibrous tissues and, ultimately, implant failure.

Stiffness-graded pieces can also be produced by the introduction of a compositional gradient. Lima et al. [24] used laser engineered net shaping (LENS<sup>TM</sup>) to consolidate a piece from biocompatible Ti, Nb and Zr elemental powders. The authors produced a stiffness-graded plate by controlling the  $\beta$ -stabilizer element along its length. No  $\beta$ -stabilizer elements were added in the center of the plate, and the amount of such elements increases from the center to both ends of the plate. Thus,  $\alpha$ ,  $\alpha + \beta$  and  $\beta$  phases were obtained from the center to both ends of the plate. Therefore, they obtained a stiffness-graded (compositionally graded) plate with low stiffness at both ends, which is desired to decrease the mismatch between the stiffness values of the bone and the implant, while a higher stiffness was kept in the center of the plate, which is thought to provide higher stability at the fracture site.

In addition to the improvement of mechanical performance, stiffness-graded materials may also be designed to influence the behavior of cells. In vitro studies have shown that migration and differentiation of cells are significantly affected by substrate stiffness. Cell migration occurs from soft regions to regions of greater rigidity

(durotaxis) [25]. For cell differentiation, a greater neurogenesis in the less-rigid regions and greater osteogenesis in regions with higher stiffness were observed [26].

The aim of this work is to report the use of LSA to produce a less-rigid surface layer in TiCP by the (meta)stabilization of less-rigid phases ( $\alpha'$  and  $\beta$ ). In a previous work, we proposed that the presence of a surface layer with lower stiffness may increase the fatigue life because this configuration can concentrate the stress inside the piece and thus decrease the level of stress at its surface [27]. Longer fatigue life is strongly desired in structural devices such as bio implants [28]. Using the analysis of single laser tracks, we also showed that the realization of the surface layer with a stiffness lower than that of the substrate depends on the type of  $\beta$ -stabilizer element introduced and the processing parameters used [17]. In this work, we report the realization of a continuous surface layer by the overlapping of single laser tracks, using Nb as the alloying element. The energy density of the laser treatment was varied, and a detailed analysis, involving the morphological, structural, microstructural and, especially, mechanical characterization of the obtained coatings, is described.

## 2- EXPERIMENTAL PROCEDURE

LSA with preplaced powder was the chosen technique for modification of the surface of the commercially pure titanium grade 2 plates. Nb, a  $\beta$ -isomorphous phase stabilizer, was selected as the alloying element. It was used a Nb powder supplied by CBMM, Brazil, with 99.9% purity and average particle size of 36  $\mu\text{m}$ . The powder preplacement method was fully described in [17]. A homogenous layer of the powder with a thickness of approximately 200  $\mu\text{m}$  on the Ti-plate surface was obtained prior to the laser processing.

A ytterbium-doped fiber laser operating at a wavelength of 1.07  $\mu\text{m}$  with an approximation of the Gaussian beam distribution mode was used to produce linear laser tracks on the material's surface. The energy density delivered by the laser beam to the material's surface, which is the heat input of the process, was calculated by [29]:

$$\text{Energy Density (J/mm}^2\text{)} = \frac{P(W)}{V(\text{mm/s}) \times D(\text{mm})}$$

where  $P$  is the laser power;  $V$  is the displacement speed of the laser beam; and  $D$  is the laser beam diameter.

Increasing energy densities were attained by varying the laser power, the displacement speed of the laser beam on the material's surface and the laser beam diameter, as displayed in Table 1. Continuous coatings were obtained by overlap single laser tracks, using a distance between the laser track centers equal to 600  $\mu\text{m}$ . The control of the displacement speed of the laser beam and the overlapping ratio (distance between neighboring laser tracks) was performed by a CNC x-y table. A protective flux of 30 l/min argon (purity class of 5.0) was used in the melting region to inhibit oxidation.

**Table 1. Laser processing parameters used to obtain the coating by LSA.**

The morphology and microstructure of single laser tracks and the continuous coatings were characterized by visible-light microscopy (VLM) and scanning electron microscopy (SEM) in the back-scattered electron (BSE) mode. These analyses were performed in the cross-section perpendicular to the direction of the laser tracks. The Nb content of the alloyed layer was estimated by energy dispersive X-ray spectrometry (EDS) microanalysis in 24 randomly chosen points at an intermediate depth for each coating. XRD analysis was used to determine the phases present in the fusion zone of the continuous coating and was performed on the surface of the coatings that were sandpapered and polished prior to XRD measurements.

The Young's modulus (E) and hardness (H) of the studied samples were determined by instrumented indentation (nanoindenter G-200, Agilent Technologies, USA, equipped with a previously calibrated Berkovich-geometry tip). All measurements were conducted using the continuous stiffness measurement (CSM) technique that provides the E and H profiles as a function of the indentation depth [30]. Two experimental strategies were used in this work. Initially, several indentations at a depth of 1500 nm were performed for the base material (BM), the heat-affected zone (HAZ) and the fusion zone (FZ) of the 24 J/mm<sup>2</sup> coating. The same conditions were used to study the mechanical properties of the FZ of all coatings. These micrometer indentation tests served to analyze the E and H of each produced layer of a given sample and for a comparison between the samples produced under different laser energies.

Subsequently, an array of 20x20 indentations at 400 nm, as shown in Figure 1, was performed on the 24 J/mm<sup>2</sup> coating. This array encompassed a square area of 150 x 150 μm<sup>2</sup>, which is large enough to include a part of the FZ and a part of the HAZ of the

coating. The obtained E and H values were displayed as colored distribution maps on the indented square area because the position of each indentation is known. These maps were used for in-depth analysis of the width of the interfacial regions as well as the effect of the microstructure on the achieved values and homogeneity achieved.

**Figure 1. VLM image showing 400 imprints performed at a 400-nm depth.**

### 3- RESULTS AND DISCUSSION

#### 3.1 Morphological, structural and microstructural characterization

Prior to obtaining the continuous coating by overlap single laser tracks, a preliminary study was performed to determine the processing parameters that could attain the conduction mode by varying the laser power, the displacement speed of the laser beam and the laser beam diameter. Figure 2 shows a VLM image of the cross-section of a laser track obtained using  $37 \text{ J/mm}^2$  of energy density, using the laser processing parameters displayed in Table 1. As can be observed, both the ZF and HAZ can be distinguished from the BM. The depth, width and reinforcement (elevation of the FZ relative to the sheet's surface) of the FZ were about 270, 1100 and 150  $\mu\text{m}$ , respectively; hence, the depth/width ratio was 0.25. Laser processing conditions that promote FZ with a depth/width ratio smaller than 0.4 are classified as conduction mode [31]. This mode, characterized by a shallower and wider FZ, shows greater stability of the melting pool [32] and is more adequate for coating purposes. All FZs obtained using energy densities in the  $24\text{-}65 \text{ J/mm}^2$  range (not shown here) exhibited the conduction mode, including that shown in Figure 2. The HAZ showed a quite constant thickness, at about 600  $\mu\text{m}$ , that was independent of the applied energy density.

**Figure 2. VLM image of the cross section of the laser track obtained using an energy density of  $37 \text{ J/mm}^2$ .**

Figure 3 shows VLM images of the 24, 37, 49 and  $65 \text{ J/mm}^2$  coatings. The metallographic preparation was performed in a plane perpendicular to the direction of the laser tracks.

**Figure 3. VLM images of the (a) 24, (b) 37, (c) 49 and (d) 65 J/mm<sup>2</sup> coatings.**

These VLM images show that the obtained coatings are practically free of cracks and porosity. The single laser tracks, which were overlapped to compose the continuous coatings, can be identified by the serrated profile observed in the interface between FZ and HAZ. The center of each laser track produced the deepest regions of the FZ, while the crossover points between the neighboring laser tracks formed the shallowest parts. By comparing the four VLM images of Figure 3, one can observe that the higher the energy density, the more pronounced is the serrated profile of the coating. The 24 and 37 J/mm<sup>2</sup> coatings showed a wavy surface, while flatter surfaces were observed in the 49 and 65 J/mm<sup>2</sup> coatings. The microstructure change in the HAZ can also be observed in these images. Grains located closer to the FZ grew considerably. Regardless of the applied energy density, the thickness of the HAZ was quite constant at about 600  $\mu\text{m}$ , close to that observed in the single laser track (see Figure 2). Figure 4 shows the depth of the FZ as a function of the energy density measured both in the center of the laser tracks (deepest region) and in the crossover points between the neighboring laser tracks (shallowest region). As expected, deeper FZs were obtained when higher energy densities were employed.

**Figure 4. Depth of the FZ as a function of the energy density.**

SEM in the BSE mode is a very suitable technique for the characterization of laser-alloyed coatings because it allows for the identification of compositional heterogeneities at distinct levels that are present in the as-processed coatings. Since the atomic mass of Nb is higher than that of Ti, the regions with a higher Nb content are

revealed by their higher relative brightness, revealing the Nb distribution throughout the FZ. Figure 5a shows a low-magnification BSE-SEM image in which the FZ of the 24 J/mm<sup>2</sup> coating can be distinguished from the substrate by its brightness. The serrated profile of the bottom of the FZ can be clearly observed. On the other hand, the BSE-SEM image shows that the contour line between the coating (brighter zone) and the substrate (bottom-side dark gray zone) is very irregular. A micropore can be observed in the bottom part of the second laser track from the left, close to the FZ-HAZ interface, corroborating the low porosity in the coating that was already observed in the VLM images. A white spot can be observed in the second laser track from the left. EDS analysis showed that it corresponds to a non-melted Nb particle. This indicates that the heat input (energy density delivered by the laser beam) was not sufficient to melt all Nb powder particles prepositioned on the substrate. Hence, considering that Nb has a higher melting point than Ti and that the enthalpy of mixing is positive in the Ti-Nb system, some non-melted Nb particles may be present after laser processing [33].

Figure 5b shows a BSE-SEM image of the 49 J/mm<sup>2</sup> coating at higher magnification, highlighting the overlap of the two neighboring laser tracks. Two levels of compositional heterogeneity can be observed better: bright regions (indicated by red arrows) concentrically arranged with the cap shape of FZ and patterns in the form of columns or cells. The concentrically arranged bright regions are frozen zones that are richer in Nb along the Marangoni convection current in the melt pool. The high cooling rate and the consequent brief time in the liquid state avoid the complete homogenization of both elements before solidification. This incomplete homogenization remained after solidification and cooling to room temperature. On the other hand, the patterns in the form of columns or cells resulted from the microsegregation of the alloying element during the solidification process. The partition coefficient of Ti-richer Ti-Nb alloys is

higher than unity [34]. This means that the solidification front rejects Ti. The constitutional supercooling breaks down the solidification front from planar to cellular. The Ti rejected by the solidification front during cellular growth accumulates in the intercellular regions, producing such columns or cells, the center of which has a higher Nb content than the borders.

The interval of time in which a point inside the FZ is held in the liquid state is related to the distance from the point to the FZ/HAZ interface. The closer the point from the FZ/HAZ interface, the shorter is the interval of time that this point was held in the liquid state. Hence, an FZ limit layer can be defined as the last region to melt and the first to solidify. At this limit layer, the very brief time in the liquid state did not allow a more homogeneous dilution of Nb and produced the irregular contour line of the alloyed zone observed in Figures 5a and 5b. Figure 5c shows the FZ/HAZ interface at higher magnification. It can be observed that it is free of micropores and nonbonded borders. Martensitic plates are observed in this region. Makuch et al. [14] also reported martensite ripples in the FZ/HAZ interface in LSA of Ti<sub>6</sub>Al<sub>4</sub>V with boron and carbon.

**Figure 5. Low-magnification SEM image of the 24 J/mm<sup>2</sup> coating (a), overlap of two laser tracks in the 49 J/mm<sup>2</sup> coating (b), and the FZ/HAZ interface of the 65 J/mm<sup>2</sup> coating (c).**

Figure 6 shows high-magnification BSE-SEM images of the typical microstructures observed in the FZ of the 24 (a), 37 (b), 49 (d) and 65 J/mm<sup>2</sup> (c) coatings. As can be observed, the chemical microsegregation, which produced a region with higher (brighter region) or lower (darker region) Nb content, is present in all coatings. The Nb content of the FZ was estimated by EDS microanalysis for 24

randomly chosen points in an intermediate depth of all coatings. The minimum and maximum values for each coating are reported in Table 2. All coatings show fluctuations of Nb content that are related to the incomplete homogenization of Ti and Nb prior to FZ solidification and the microsegregation, as shown above. Moreover, the Nb content is related to the heat input. Greater heat input means greater substrate fusion, increasing the dilution and thus producing a coating with a lower Nb content. This relationship between the Nb content and heat input was already demonstrated in our previous works [17, 27].

**Figure 6. Typical microstructures observed in the FZ of the coatings obtained with 24 (a), 37 (b), 49 (c) and 65 J/mm<sup>2</sup> (d) of energy density.**

**Table 2. Maximum and minimum values estimated for each coating.**

The phases present in the FZ could be identified by correlating the microstructures observed by BSE-SEM, the Nb content determined by EDS analyses and the XRD patterns. Such identification is only possible if the volume fraction of the phase to be identified is above the detection limit of the SEM and XRD techniques. The microstructure of the 24 J/mm<sup>2</sup> coating (see Figure 6a) shows needles located in the darker region and the brighter region appears to be single-phase. The XRD pattern of this coating (see Figure 7) reveals a high content of  $\beta$  phase with a smaller amount of  $\alpha''$  phase. In view of this, we can affirm that the microstructure of the 24 J/mm<sup>2</sup> coating is composed of needles of the orthorhombic martensite phase ( $\alpha''$ ) immersed in the  $\beta$  phase. Lütjering and Williams [35] related that the  $\beta$  phase was fully retained in Ti-Nb alloys with a Nb content greater than 36 %<sub>in mass</sub> that were thermally treated above  $\beta$ -

*transus* and water quenched, while the  $\alpha''$  phase was observed in Ti-Nb alloys with a Nb content greater than 10.5 %<sub>in mass</sub>. For a Nb content lesser than 10.5%, the  $\alpha'$  phase is predominantly formed. Coexistence of these phases is possible for a Nb content close to these limits. In view of this, we can suppose that the Nb content of the brighter region was sufficiently high to (meta)stabilize the  $\beta$  phase, while the lower Nb content of the darker region allowed the partial martensitic transformation only in this region.

**Figure 7. XRD patterns of the 24, 37, 49 and 65 J/mm<sup>2</sup> coatings.**

The microstructure of the 37 J/mm<sup>2</sup> coating (see Figure 6b) also presents an acicular phase immersed in a monophasic matrix, but in this case, the acicular phase is extensively dispersed in both the darker and brighter regions. To some degree, the amount of martensite lamellae is greater in the darker region. The XRD pattern of this coating also reveals a high  $\beta$  phase content, but the peaks related to the  $\alpha''$  phase are somewhat more intense compared to the XRD patterns of the 24 J/mm<sup>2</sup> coating. Moreover, some  $\alpha/\alpha'$  peaks were detected, indicating that the martensitic  $\alpha'$  phase was also formed in this coating. The Nb content in the brighter, Nb-rich region was not high enough to fully (meta)stabilize the  $\beta$  phase in this region. Moreover, the Nb content in the darker, Nb-poor region may have allowed the precipitation of both the orthorhombic ( $\alpha''$ ) and the hexagonal ( $\alpha'$ ) martensitic phases. Hence, the acicular phase should correspond to a mix of  $\alpha''$  and  $\alpha'$  phases, both immersed in a  $\beta$  phase matrix. Even though the  $\alpha'$  and  $\alpha''$  phases cannot be distinguished by SEM images, we can suppose that the  $\alpha'$  phase content must be concentrated in the darker region due to its lower Nb content.

On the other hand, the microstructure of the coatings obtained with higher energy densities (49 and 65 J/mm<sup>2</sup>) predominantly consists of an acicular phase, as shown in Figures 6c and 6d. The microstructures of both coatings appear to be independent of the brightness, that is, independent of the Nb content, obviously in the range of the Nb variation of these coatings (Table 2). The XRD patterns of these coatings (Figure 7) reveal a highly intense  $\alpha/\alpha'$  peak, indicating that the acicular phase corresponds to martensite  $\alpha'$ . However, some smaller peaks related to  $\alpha''$  are also observed. Typically, only the  $\alpha'$  phase is observed in Ti-Nb alloys with a Nb content below 10.5 % that are treated above  $\beta$ -*transus* and water quenching. However, the presence of oxygen can move the start line of the martensitic transformation to a lower temperature and consequently move the limit between the phases ( $\alpha'/\alpha''$  and  $\alpha''/\beta$ ) to a lower Nb content [36]. Moreover, some peaks related to the body-centered cubic (bcc) Nb structure were identified in the XRD patterns of the 49 and 65 J/mm<sup>2</sup> coatings. At first glance, one can suppose that these XRD peaks should be related to the  $\beta$  phase of the Ti-Nb alloy, indicating that some amount of this phase was retained in the FZ microstructure after cooling. However, we should consider that non-melted Nb particles may be present in the alloyed zone after laser processing, as observed in Figure 5a. The XRD peaks related to the bcc Nb structure may be present in all XRD patterns of Figure 7 but cannot be discerned in the XRD patterns of the 24 and 37 J/mm<sup>2</sup> coatings because they were overlapped by the XRD peaks related to the  $\beta$  phase of Ti, which were undoubtedly present in these lower-energy-density coatings. Considering that the technical literature does not report retainment of the  $\beta$  phase in Ti-Nb alloys with similar composition (low Nb content), we assigned these peaks to the presence of non-melted Nb particles.

The  $\omega$  phase was neither observed by microscopy analyses nor detected by XRD in any of the coatings. Some authors have reported  $\omega$  phase suppression due to the presence of oxygen [37]. The level of oxygen contamination in LSA with preplaced powders may have been sufficient for the suppression of the  $\omega$  phase. However, future TEM analyses are necessary to clarify this point.

### 3.2 Mechanical characterization

Figure 8 shows the E and H profiles acquired in the BM in the FZ and HAZ of the 24 J/mm<sup>2</sup> coating. The E value for the surface layer is lower than those of the HAZ and BM. Despite its lower E, the H of the surface layer is greater than two times that of the BM. The higher H and lower E agree with values reported in our previous studies [17, 27] related to single laser tracks. It was confirmed that a less-rigid continuous coating can be achieved by introducing a chemical gradient that can stabilize the  $\alpha''$  and  $\beta$  phases, which are widely known to exhibit lower E values than the  $\alpha$  and  $\alpha'$  phases. The low values of E of the coating suggest the absence of the  $\omega$  phase. The metallurgical aspects that caused the decrease in E and increase in H are described fully in [27].

Related to the HAZ, its E is statistically similar and its H is higher than that of the BM. Markovsky and Semiatin [38] demonstrated an increase in the tensile strength of commercially pure titanium after local rapid heat treatment. They attributed the strengthening to the formation of substructure, martensite and residual stresses during fast heating and cooling. The same strengthening mechanisms can be present in the HAZ of coatings obtained by LSA, which can explain the observed increase in H.

**Figure 8. E and H profiles, measured in the FZ, HAZ and BM of the 24 J/mm<sup>2</sup> coating.**

Figure 9 displays the E and H values obtained in the FZs of the four studied coatings. The E and H values of the BM are also plotted for comparison. The values related to the HAZ are suppressed in these graphs for a better visualization of the data. Furthermore, these results were averaged between the depths of 500 and 750 nm and are summarized in Table 3. All coatings show lower E and higher H compared to the BM. The coatings obtained with lower energy densities (24 and 37 J/mm<sup>2</sup>) present the lowest E values. Both lower-energy-density coatings have microstructures predominantly composed of the  $\alpha''$  phase immersed in the  $\beta$  phase, and these phases were (meta)stabilized by the relatively high Nb content, as shown previously. On the other hand, the coatings obtained with higher energy densities (49 and 65 J/mm<sup>2</sup>) exhibit intermediate E values and their microstructures are largely composed of the  $\alpha/\alpha'$  phase, for which the E value is higher than those of the  $\alpha''$  and  $\beta$  phases [39]. As shown by Aleixo et al. [40], E of the  $\alpha'$  phase depends on the Nb content in rapid-quenched Ti-Nb alloys. E decreases with increasing Nb content, reaching a minimum of approx. 66 GPa for 15 %<sub>in mass</sub> Nb when rapidly quenched from the  $\beta$ -phase field. Thus, the presence of the  $\alpha'$  phase with Nb in solid solution in the FZ of the coating would also decrease its E value. On the other hand, the difference between the H values of the various coatings was not statistically significant.

**Figure 9. E and H as functions of the indentation depth, related to the FZ of the coatings obtained with different energy densities, compared to the same properties of the BM.**

**Table 3. Summary of the obtained E and H for each analyzed coating. Values were calculated in a depth range of 500-750 nm.**

The E values were influenced by the amount of Nb introduced in the alloyed zone because the higher Nb contents of the 24 and 37 J/mm<sup>2</sup> coatings allowed the (meta)stabilization of the less-rigid phases ( $\beta$  and  $\alpha''$ ). The relationship between the changes in mechanical properties (decrease in E and increase in H) and the amount of Nb introduced in the alloy can be extended to the heat input. As stated before, the higher the heat input, the higher is the dilution of the alloying element because a larger volume of substrate was fused. Hence, the higher the heat input, the lower is the amount of Nb at the alloyed layer. Therefore, the energy density of the laser processing must be controlled to produce an adequate dilution that is able to (meta)stabilize the  $\beta$  and  $\alpha''$  phases.

The relationship between the energy density of the laser processing, the dilution of the alloying element and the (meta)stabilization of the less-rigid phases was already demonstrated in our previous works [17, 27] in which the heat input was controlled only by the changes in the laser power. In the present work, the control of the heat input was broader because the laser power, the displacement speed of the laser beam and the laser beam diameter were all changed, and yet the previously obtained relationship was still corroborated.

Previous nanoindentation results allowed us to determine the E and H properties of each individual layer, demonstrating the decrease in E in the alloyed coating with respect to the BM, which also depends on the energy density of the laser surface treatment. Nevertheless, it is expected that the mechanical features of the whole material also depend on the width of the generated interfaces, that is, on the depth gradient of mechanical properties. This is especially important when the material is under dynamic loading conditions and hence is susceptible to fatigue failure. In this sense, a

homogeneous distribution of mechanical features with a smooth gradient in the interfacial regions should be desirable. In view of this, property maps (see Figure 10) were constructed by plotting the E and H values acquired from a matrix of 400 indentations (see Figure 1). Our choice of the 24 J/mm<sup>2</sup> coating was due to its lower E and higher H. The colored maps show that the coating shows more homogenous values of E and H than the HAZ, indicating the adequate solute distribution and, consequently, an almost uniform phase dispersion in the coating despite the compositional heterogeneity showed by the BSE-SEM analyses (Figures 5 and 6). Furthermore, E is gradually reduced and H is gradually increased in the interface region, from the HAZ toward the coating, which is consistent with the concept of FGM.

**Figure 10. E (a) and H (b) colored maps with the 400 microscopic imprints inside a square area of 150 x 150 μm<sup>2</sup>.**

#### 4- Conclusions

Using energy densities in the 24-65 J/mm<sup>2</sup> range, continuous coatings were obtained by overlapping laser tracks. The coatings are practically free of cracks and porosity. A quite constant HAZ, at about 600 μm, was observed, independent of the applied energy density.

The most outstanding microstructural heterogeneities observed in the coatings were some remaining non-melted Nb particles, incomplete compositional homogenization before FZ solidification and chemical microsegregation.

The phases present in the FZ were identified by XRD and SEM analyses. Both the 24 and 36 J/mm<sup>2</sup> coatings present microstructures predominantly composed by martensitic lamellae of the α'' phase immersed in the β phase. A small amount of the α' phase is present in the FZ of the 36 J/mm<sup>2</sup> coating. Both the 49 and 65 J/mm<sup>2</sup> coatings show microstructures largely composed of the α/α' phase, with some α'' phase.

Instrumented indentation showed that all coatings exhibit E values lower than that of the substrate. Also, the H values of all coatings are significantly higher than that of the substrate.

The decrease in the stiffness of the coating was related to the heat input and the phases formed in the FZ. Lower energy densities promoted the fusion of a smaller volume of the substrate, decreasing the dilution of the alloying element. Hence, a higher amount of Nb introduced in the FZ of the lower-energy-density coatings allowed the (meta)stabilization of the β and α'' phases, for which the values of Young's modulus are lower than those of the α and α' phases. On the other hand, higher energy densities produced a coating with a lower amount of Nb, and the microstructure consisting largely of the α/α' phase resulted in a smaller decrease in E.

Nanoindentation analysis also showed the phase dispersion achieved in the 24 J/mm<sup>2</sup> coating produced relatively homogenous values of E and H in the FZ despite the compositional heterogeneity, and a gradual change in these properties through the HAZ/FZ interface.

### **Future works**

Future works, already in progress, consist of first measuring the residual stress of the less-rigid coating in the as-processed state and the use of heat treatment to change/improve some of the coating features; later, the coating in the optimized state will be fatigue tested. In parallel, we are investigating the feasibility of applying the less-rigid Ti-Nb coating to orthopedic implants through measurement of its cytocompatibility, osseointegration ability and corrosion behavior in simulated body fluid.

### **ACKNOWLEDGEMENTS**

The authors gratefully acknowledge the São Paulo State Research Foundation (FAPESP, Brazil) (Grant 2011/19982-2) for its financial support.

## References

- [1] J. Miyamoto, M. Niino, M. Koizumi, FGM research programs in Japan-from the structural to functional uses, in: I. Shiota, Y. Miyamoto (Eds.), *Functionally Graded Materials 1996*, Elsevier, Netherland, 1997, pp. 1-8. ISBN 978-0-08-053209-7.
- [2] R.M. Mahamood, E.T.Akinlabi, *Functionally Graded Materials*, first ed., Springer, Switzerland, 2017. ISBN 978-3-319-53756-6.
- [3] A. Sola, D. bellucci, V. Cannillo, Functionally graded materials for orthopedic applications-an update on design and manufacturing, *Biotechnol. Adv.* 34 (2016) 504-531.
- [4] R.M. Mahamood, E.T.Akinlabi, M. Shukla, S. Pityana, *Functionally Graded Materials: An overview*, in: *Proceedings of the World Congress on Engineering WCE-2012 3* (2012) 1593-1597.
- [5] E.S.N. Lopes, R.J. Contieri, S.T. Button, R. Caram, Femoral hip stem prosthesis made of graded elastic modulus metastable  $\beta$  Ti Alloy, *Mater. Design* 69 (2015) 30–36.
- [6] M. Nakai, M. Niinomi, X. Zhao, X. Zhao, Self-adjustment of Young's modulus in biomedical titanium alloys during orthopaedic operation, *Mater. Lett.* 65 (2011) 688-690.
- [7] Z. Liu, M.A. Meyers, Z. Zhang, R.O. Ritchie, Functional gradients and heterogeneities in biological materials: design principles, functions, and bioinspired applications, *Prog. Mater. Sci.* 88 (2017) 467-498.
- [8] L.J. Gibson, M.F. Ashby, *Cellular solids: structure and properties*, second ed., Cambridge University Press, U.K., 1997. ISBN 978-1-139-87832-6.
- [9] W.M. Steen, J. Mazumder, *Laser material processing*, Springer, London, 2010. ISBN 978-1-84996-062-5.

- [10] J.D. Majumdar, B.L. Mordike, I. Manna, Friction and wear behavior of Ti following laser surface alloying with Si, Al and Si+Al, *Wear* 242 (2000) 18–27.
- [11] A.I.P. Nwobu, R. D.Rawlings, D.R.F. West, Nitride formation in titanium based substrates during laser surface melting in nitrogen–argon atmospheres, *Acta Mater.* 47 (1999) 631-643.
- [12] C. Chen, M. Zhang, S. Zahng, Q. Chang, H. Ma, Surface oxygen diffusion hardening of TA2 pure titanium by pulsed Nd: YAG laser under different gas atmosphere, in: S. Hinduja, L. Li (Eds.), *Proceedings of the 36th International MATADOR Conference*, Springer, London, U.K., 2010.
- [13] B. Courant, J.J. Hantzpergue, L. Avril, S. Benayoun, Structure and hardness of titanium surface carburized by pulsed laser melting with graphite addition, *J. Mater. Process. Technol.* 160 (2005) 374-381.
- [14] N. Makuch, M. Kulka, P. Dziarski, D. Przystacki, Laser surface alloying of commercially pure titanium with boron and carbon, *Opt. Laser Eng.* 57 (2014) 64-81.
- [15] R. Filip, Alloying of surface layer of the Ti-6Al-4V titanium alloy through the laser treatment, *J. Achiev. Mater. Manuf. Eng.* 15 (2006) 174-180.
- [16] A.F. Saleh, J.H. Abboud, K.Y. Benyounis, Surface carburizing of Ti-6Al-4V alloy by laser melting, *Opt. Laser Eng.* 48 (2010) 257-267.
- [17] J.B. Fogagnolo, A.V. Rodrigues, E. Sallica-Leva, M.S.F. Lima, R. Caram, Surface stiffness gradient in Ti parts obtained by laser surface alloying with Cu and Nb, *Surf. Coat. Technol.* 297 (2016) 34-42.
- [18] T. Tan, N. Rahbar, S.M. Allameh, S. Kwofie, D. Dissmore, K. Ghavami, W.O. Soboyejo, Mechanical properties of functionally graded hierarchical bamboo structures, *Acta Biomater.* 7 (2011) 3796-3803.
- [19] V.K. Ganesh, K. Ramakrishna, D.N. Ghista, Biomechanics of bone-fracture fixation by stiffness-graded plates in comparison with stainless-steel plates, *Biomed. Eng. Online* 4 (2005) 46. DOI: 10.1186/1475-925X-4-46.

- [20] H. Fouad, In vitro evaluation of stiffness graded artificial hip joint femur head in terms of joint stresses distributions and dimensions: finite element study, *J. Mater. Sci. Mater. Med.* 22 (2011) 1589-1598.
- [21] K.A. Nazari, T. Hilditch, M.S. Dargusch, A. Nouri, Functionally graded porous scaffolds made of Ti-based agglomerates, *J. Mech. Behav. Biomed. Mater.* 63 (2016) 157-163.
- [22] M. Fousová, D. Vojtěch, J. Kubásek, E. Jablonská, J. Fojt, Promising characteristics of gradient porosity Ti-6Al-4V alloy prepared by SLM process, *J. Mech. Behav. Biomed. Mater.* 69 (2017) 368-376.
- [23] I.H. Oh, H. Segawa, N. Nomura, S. Hanada, Microstructures and mechanical properties of porosity-graded pure titanium compacts, *Mater. Trans.* 44 (2003) 657-660.
- [24] D.D. Lima, S.A. Mantri, C.V. Mikler, R. Contieri, C.J. Yannetta, K.N. Campo, E.S. Lopes, M.J. Styles, T. Borkar, R. Caram, R. Banerjee, Laser additive processing of a functionally graded internal fracture fixation plate, *Mater. Design* 130 (2017) 8–15.
- [25] J. Hong, J. Kim, J. Baek, M. Cha, J. Lee, S. Park, Cell Migration Driven by a Mechanical Stiffness Gradient, *Proceedings of the 2nd IEEE International Conference on Nano/Micro Engineered and Molecular Systems*, Bangkok, Thailand, 2007.
- [26] T.H. Kim, D.B. An, S.H. Oh, M.K. Kang, H.H. Song, J.H. Lee, Creating stiffness gradient polyvinyl alcohol hydrogel using a simple gradual freezing–thawing method to investigate stem cell differentiation behaviors, *Biomaterials* 40 (2015) 51-60.
- [27] J.B. Fogagnolo, A.V. Rodrigues, M.S.F. Lima, V. Amigó, R. Caram, A novel proposal to manipulate the properties of titanium parts by laser surface alloying, *Scr. Mater.* 68 (2013) 471-474.
- [28] S.H. Teoh, Fatigue of biomaterials: a review, *Int. J. Fatigue* 22 (2000) 825–837.
- [29] K. Antony, N. Arivazhagan, Studies on energy penetration and Marangoni effect during laser melting process, *J. Eng. Sci. Technol.* 10 (2015) 509-525.

[30] E. Rayón, V. Bonache, M.D. Salvador, E. Bannier, E. Sánchez, A. Denoirjean, H. Ageorges, Nanoindentation study of the mechanical and damage behaviour of suspension plasma sprayed TiO<sub>2</sub> coatings, *Surf. Coat. Technol.* 206 (2012) 2655-2660.

[31] D.C. Weckman, H.W. Kerr, J.T. Liu, The effects of process variables on pulsed Nd: YAG laser spot welds: Part II. AA 1100 aluminum and comparison to AISI 409 stainless steel, *Metall. Mater. Trans. B* 28 (1997) 687-700.

[32] A.M. Chelladurai, K.A. Gopal, S. Murugan, S. Venugopal, T. Jayakumar, Energy transfer modes in pulsed laser seam welding, *Mater Manuf. Process.* 30 (2015) 162-168.

[33] M. Calin, A. Gebert, A.C. Ghinea, P.F. Gostin, S. Abdi, C. Mickel, J. Eckert, Designing biocompatible Ti-based metallic glasses for implant applications, *Mater. Sci. Eng. C* 33 (2013) 875-883.

[34] A. Cremasco, P.N. Andrade, R.J. Contieri, E.S.N. Lopes, C.R.M. Afonso, R. Caram, Correlations between aging heat treatment,  $\omega$  phase precipitation and mechanical properties of a cast Ti-Nb alloy, *Mater. Design* 32 (2011) 2387-2390.

[35] G. Lütjering, J.C. Williams, *Titanium*, second ed., Springer, Germany, 2010. ISBN 978-3-540-73036-1.

[36] W.Y. Kim, H.S. Kim, Effect of oxygen content on microstructure and mechanical properties of Ti-Nb-Ge alloys for biomedical application, *Adv. Mater. Res.* 47 (2008) 1450-1453.

[37] J.G. Niu, D.H. Ping, T. Ohno, W.T. Geng, Suppression effect of oxygen on the  $\beta$  to  $\omega$  transformation in a  $\beta$ -type Ti alloy: insights from first-principles, *Model. Simul. Mater. Sci. Eng.* 22 (2014) 015007.

[38] P.E. Markovsky, S.L. Semiatin, Microstructure and mechanical properties of commercial-purity titanium after rapid (induction) heat treatment, *J. Mater. Process. Technol.* 210 (2010) 518-528.

[39] C.M. Lee, C.P. Ju, J.H. Chern-Lin, Structure-property relationship of cast Ti–Nb alloys, *J. Oral Rehabil.* 29 (2002) 314-322.

[40] G.T. Aleixo, C.R.M. Afonso, A.A. Coelho, R. Caram, Effect of omega phase on elastic modulus of Ti-Nb alloys as a function of composition and cooling rate, *Solid State Phenom.* 138 (2008) 393-398.

### Figure captions

**Figure 1. VLM image showing 400 imprints performed at a 400-nm depth.**

**Figure 2. VLM image of the cross section of the laser track obtained using an energy density of 37 J/mm<sup>2</sup>.**

**Figure 3. VLM images of the (a) 24, (b) 37, (c) 49 and (d) 65 J/mm<sup>2</sup> coatings.**

**Figure 4. Depth of the FZ as a function of the energy density.**

**Figure 5. Low-magnification SEM image of the 24 J/mm<sup>2</sup> coating (a), overlap of two laser tracks in the 49 J/mm<sup>2</sup> coating (b), and the FZ/HAZ interface of the 65 J/mm<sup>2</sup> coating (c).**

**Figure 6. Typical microstructures observed in the FZ of the coatings obtained with 24 (a), 37 (b), 49 (c) and 65 J/mm<sup>2</sup> (d) of energy density.**

**Figure 7. XRD patterns of the 24, 37, 49 and 65 J/mm<sup>2</sup> coatings.**

**Figure 8. E and H profiles, measured in the FZ, HAZ and BM of the 24 J/mm<sup>2</sup> coating.**

**Figure 9. E and H as functions of the indentation depth, related to the FZ of the coatings obtained with different energy densities, compared to the same properties of the BM.**

**Figure 10. E (a) and H (b) colored maps with the 400 microscopic imprints inside a square area of 150 x 150 μm<sup>2</sup>.**

Table 1. Laser processing parameters used to obtain the coating by LSA.

	Energy density (J/mm <sup>2</sup> )	Laser power (W)	Laser beam diameter (mm)	Displacement speed of the laser beam (mm/s)
24 J/mm <sup>2</sup> coating	24.4	400	1.64	10
37 J/mm <sup>2</sup> coating.	36.6	300	1.64	5
49 J/mm <sup>2</sup> coating	48.8	400	1.64	5
65 J/mm <sup>2</sup> coating	65.0	400	0.82	7.5

Table 2. Maximum and minimum values estimated for each coating.

	Nb content (in mass%)
24 J/mm <sup>2</sup> coating	26.2 – 32.3
37 J/mm <sup>2</sup> coating	19.7 – 26.4
49 J/mm <sup>2</sup> coating	10.5 – 13.1
65 J/mm <sup>2</sup> coating	6.5 – 8.8

Table 3. Summary of the obtained E and H for each analyzed coating. Values were calculated in a depth range of 500-750 nm.

Coating	E (GPa)	Std. Dev.	H (GPa)	Std. Dev.
Base material	124	3.5	2.40	0.22
24 J/mm <sup>2</sup> coating	99	5.3	6.20	0.51
37 J/mm <sup>2</sup> coating	102	6.5	5.94	0.70
49 J/mm <sup>2</sup> coating	109	3.9	5.07	0.15
65 J/mm <sup>2</sup> coating	110	1.4	4.87	0.11

Figure 1  
[Click here to download high resolution image](#)

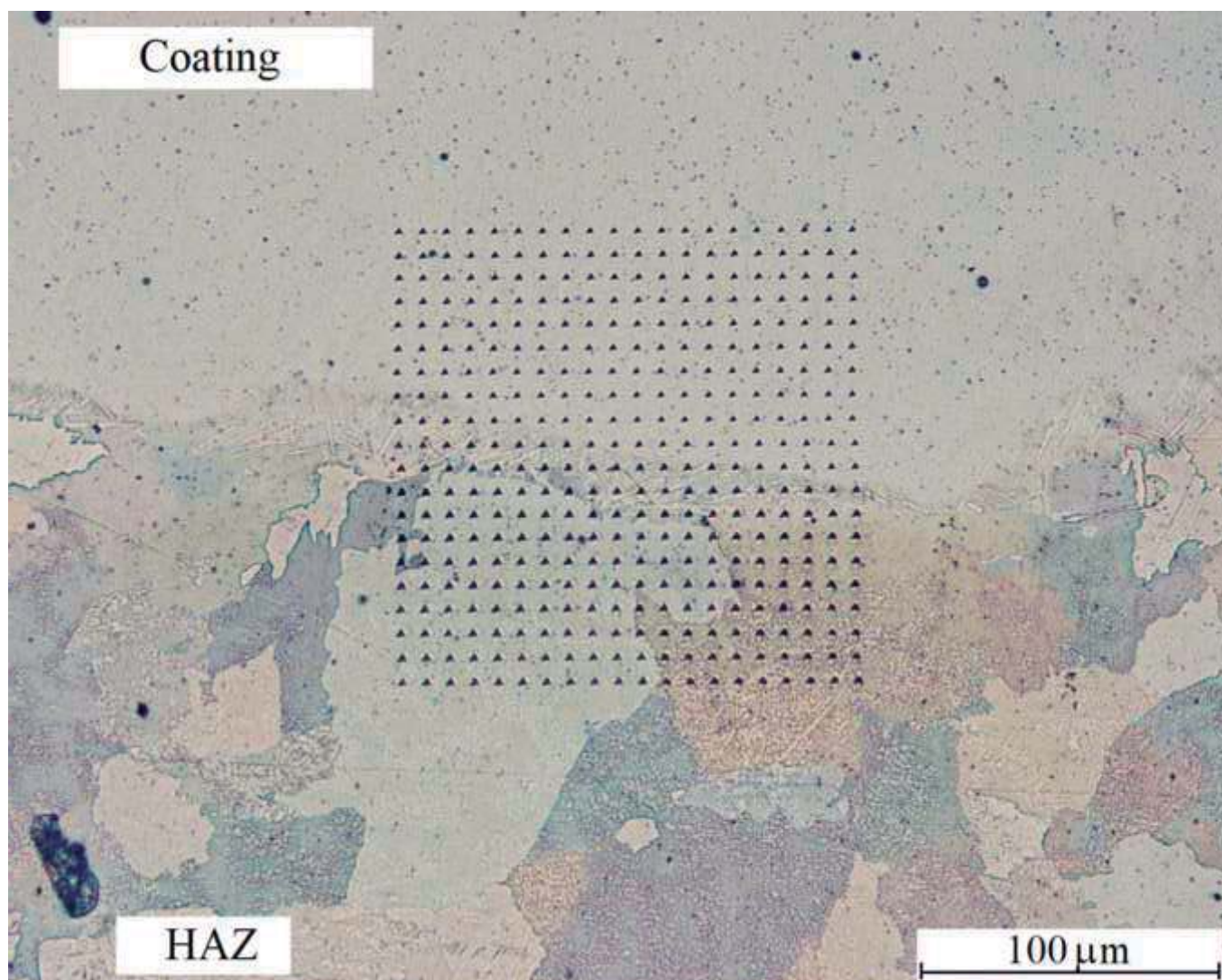


Figure 2  
[Click here to download high resolution image](#)

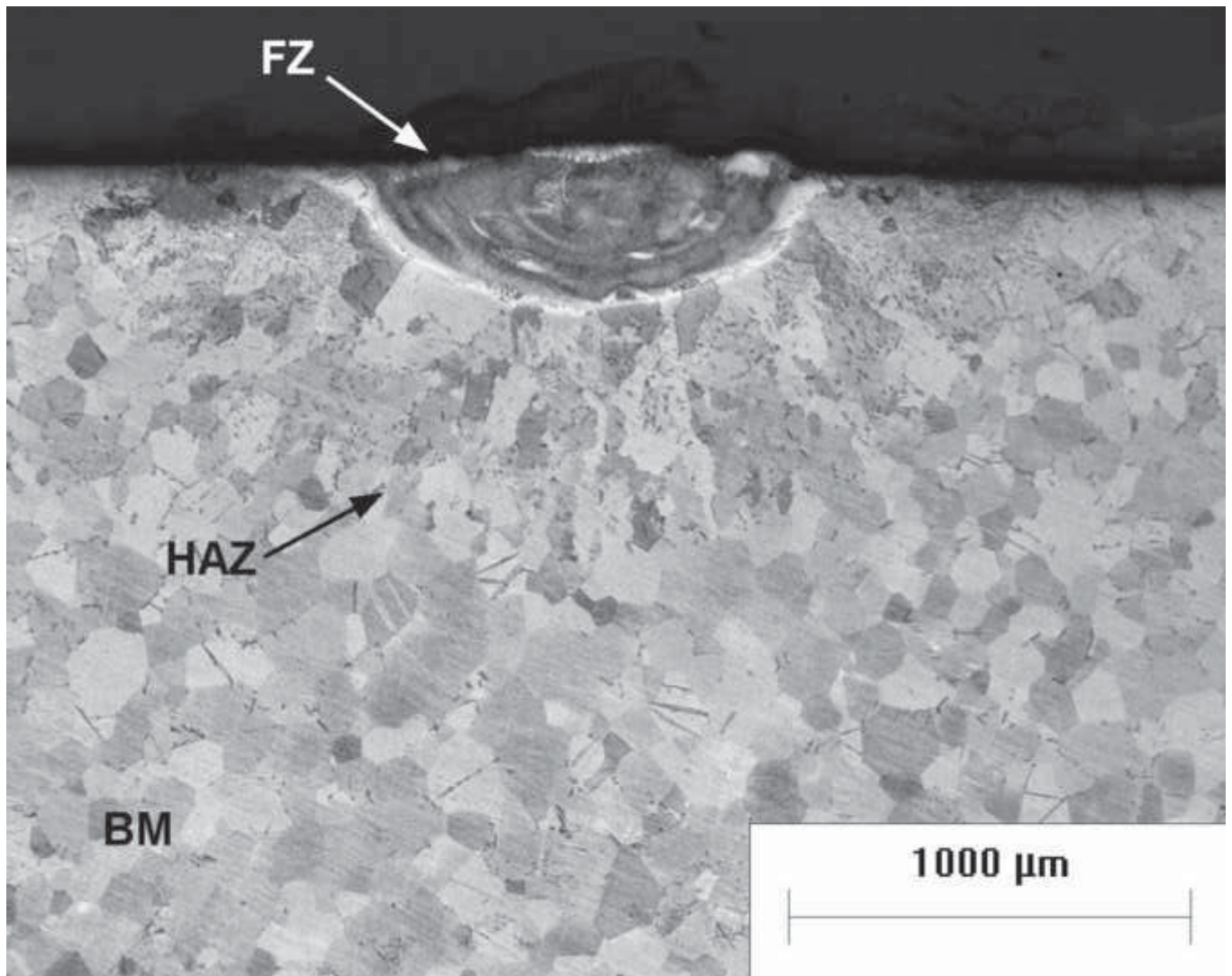


Figure 3a  
[Click here to download high resolution image](#)

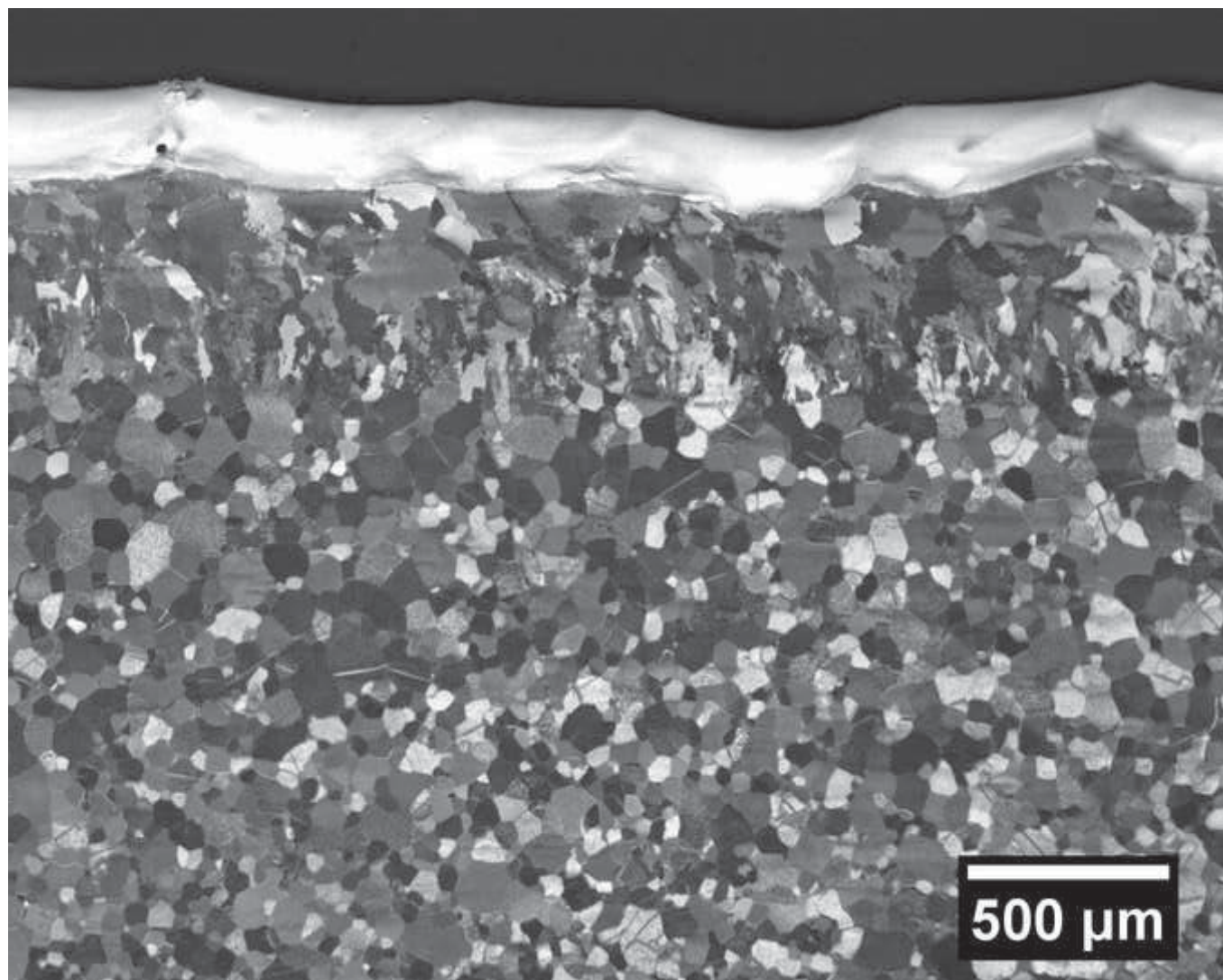


Figure 3b  
[Click here to download high resolution image](#)

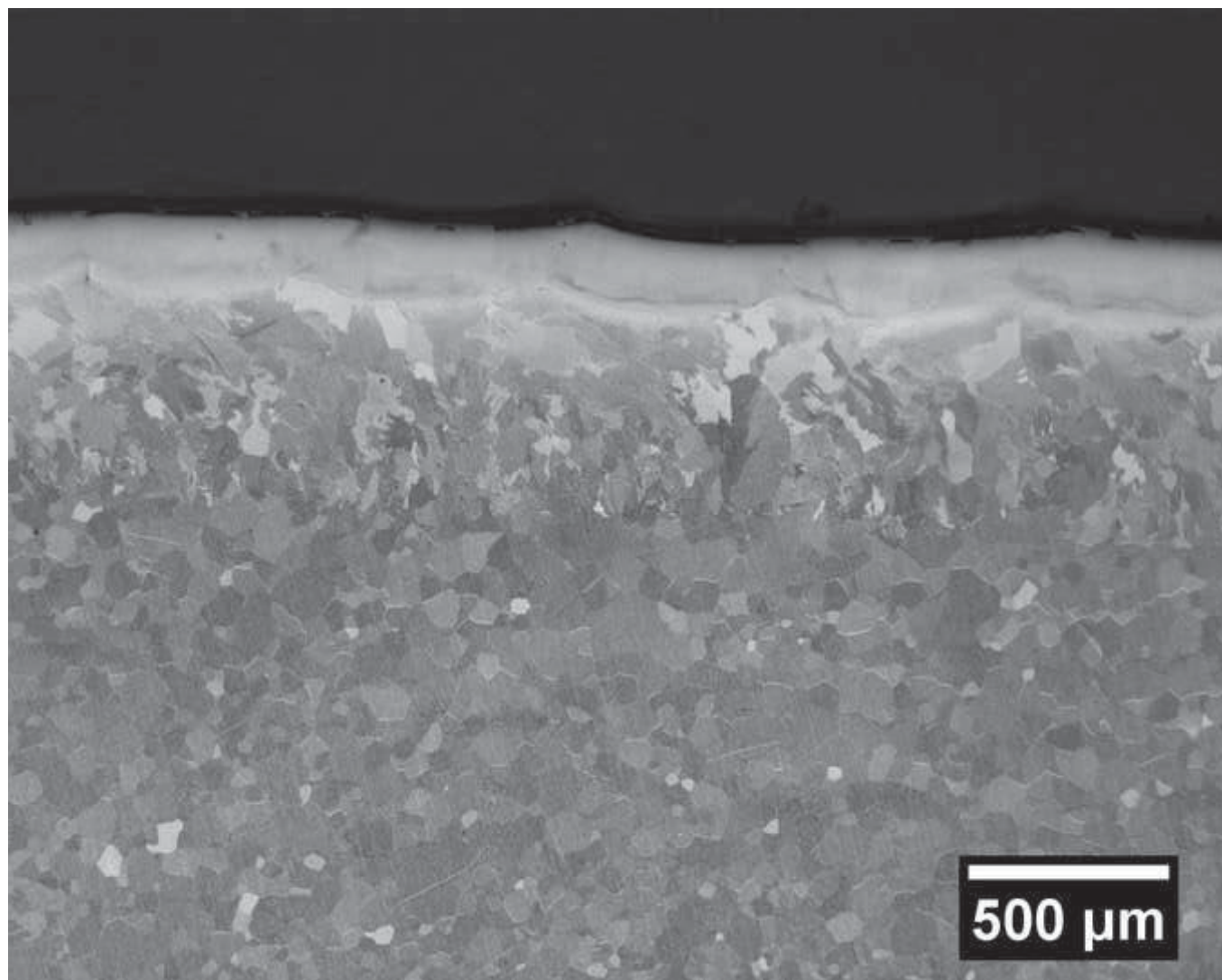


Figure 3c  
[Click here to download high resolution image](#)

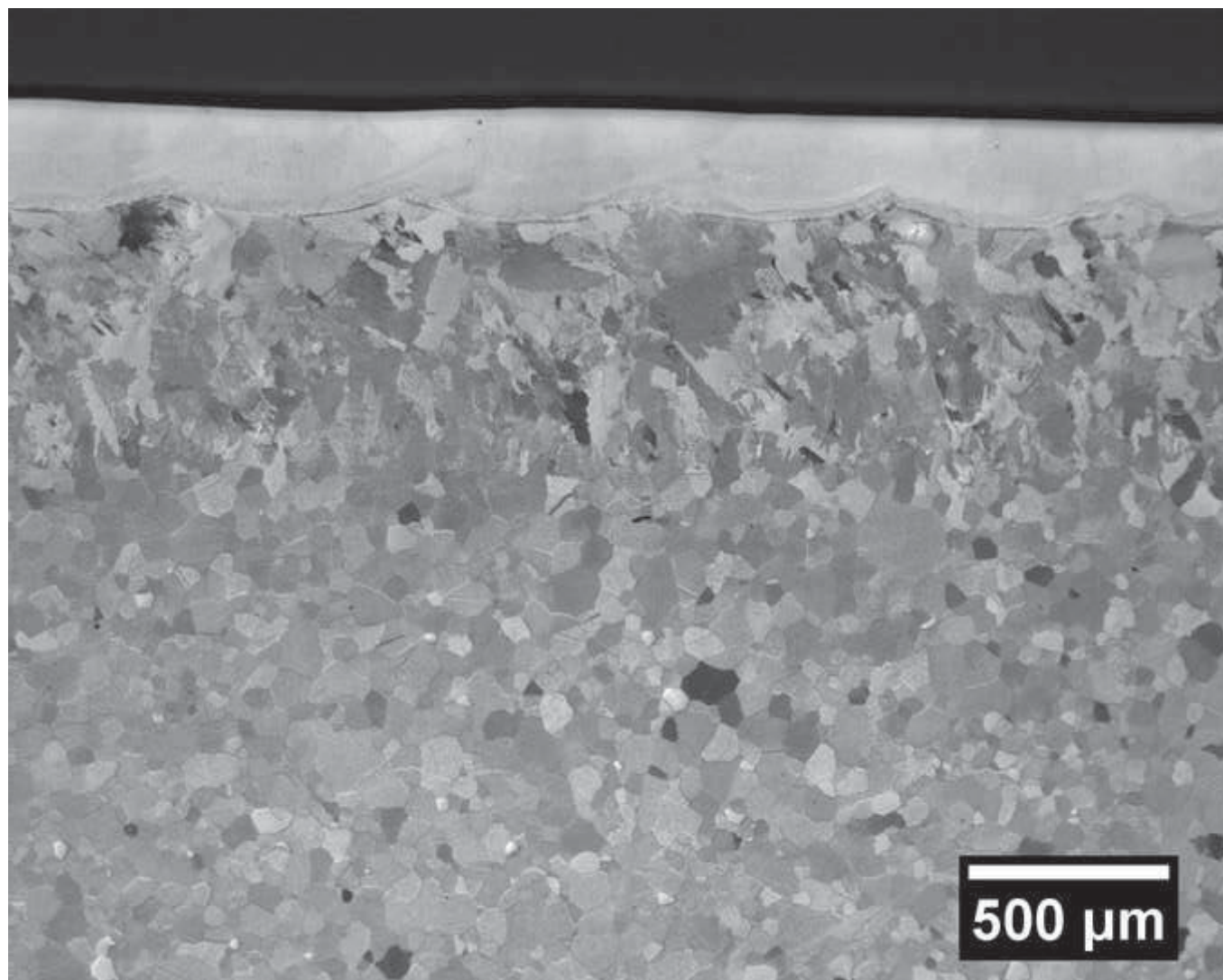


Figure 3d  
[Click here to download high resolution image](#)

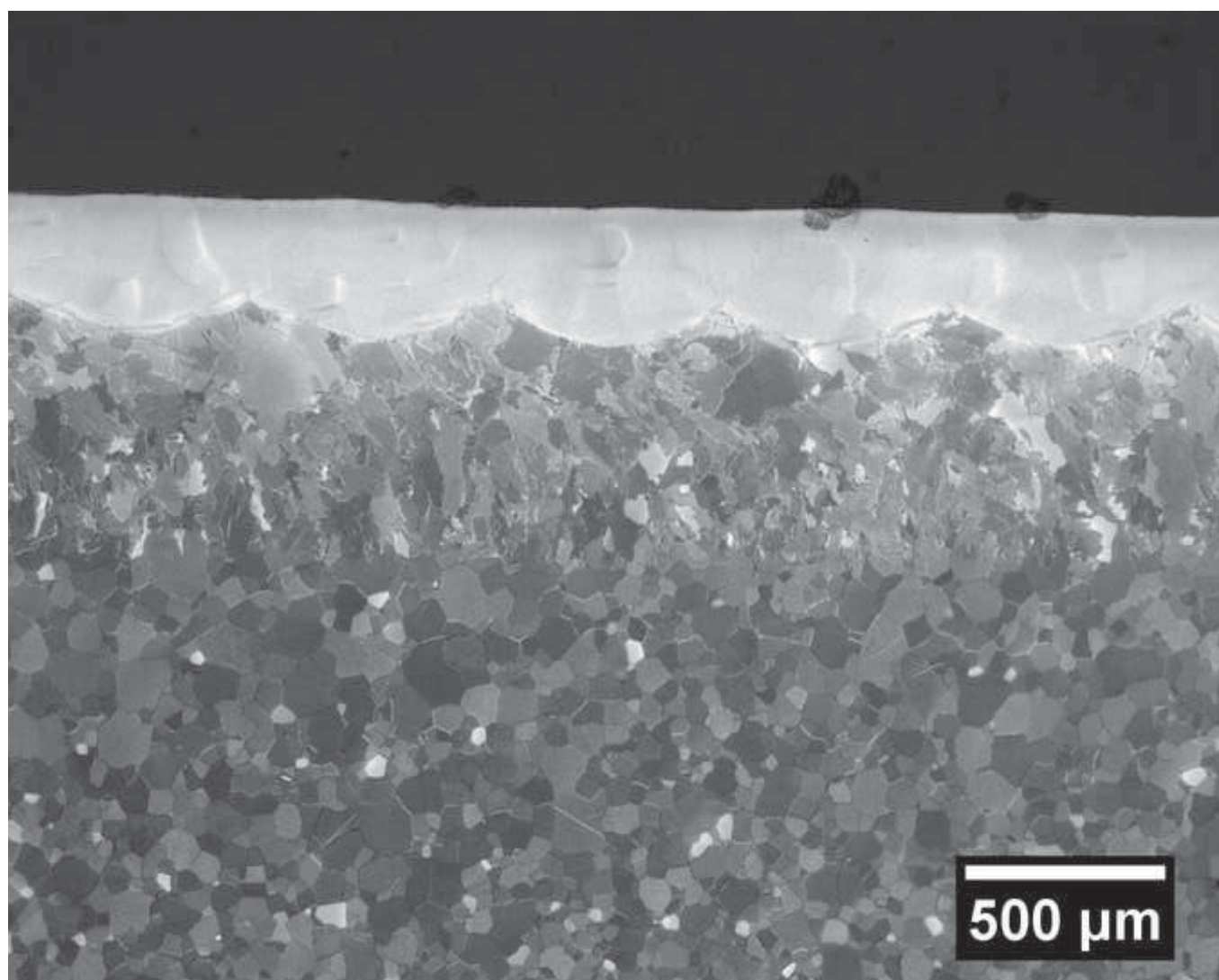


Figure 4  
[Click here to download high resolution image](#)

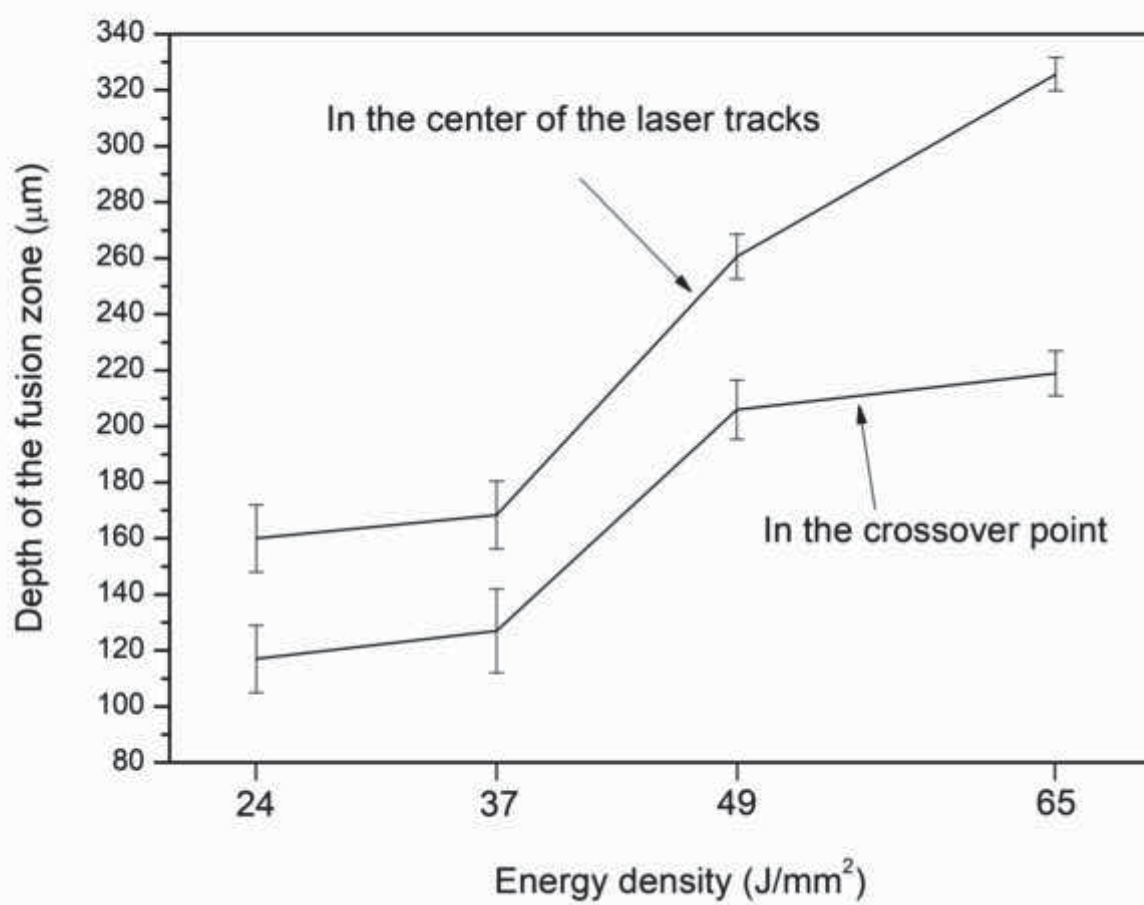


Figure 5a  
[Click here to download high resolution image](#)

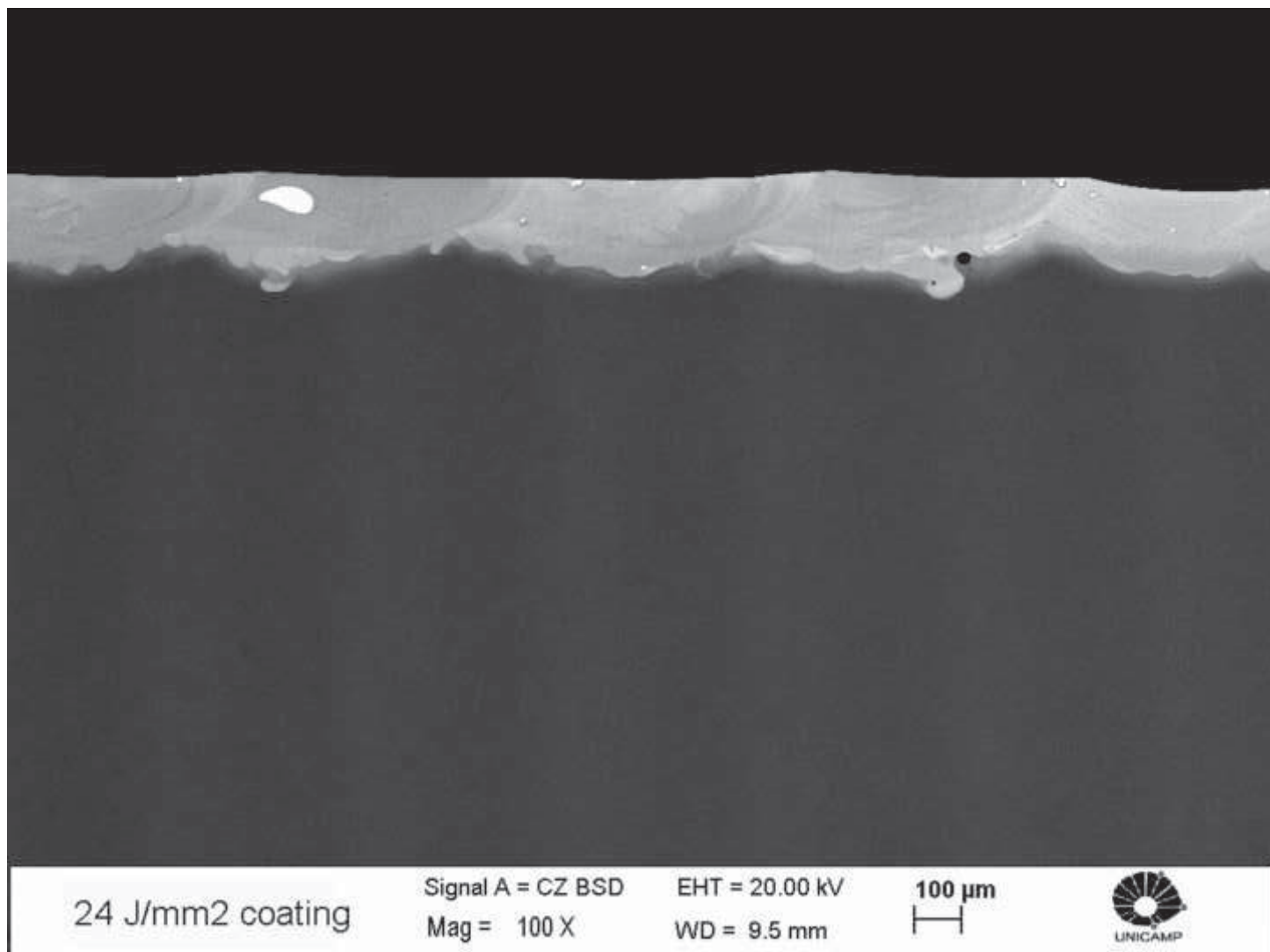


Figure 5b  
[Click here to download high resolution image](#)

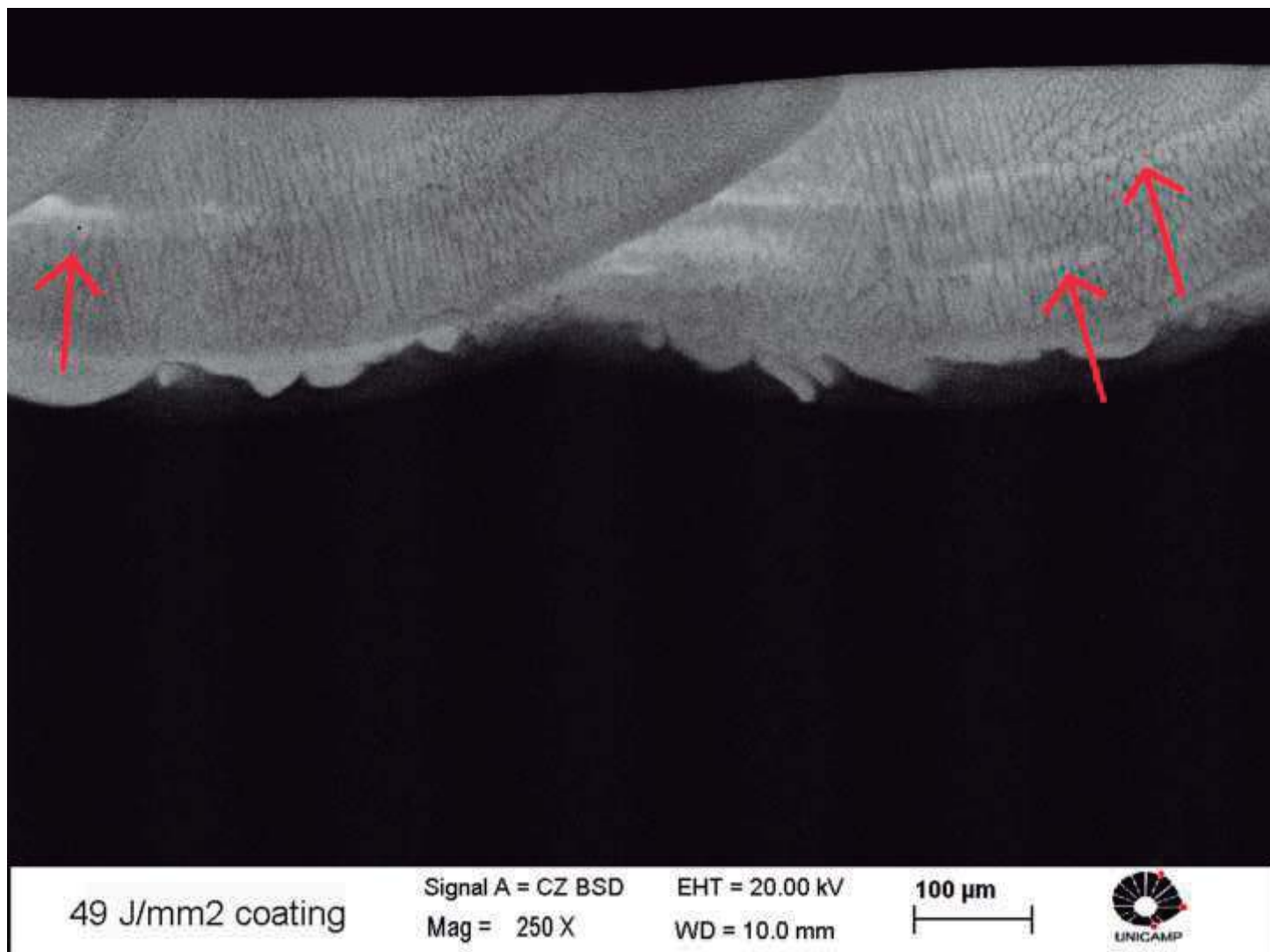


Figure 5c  
[Click here to download high resolution image](#)

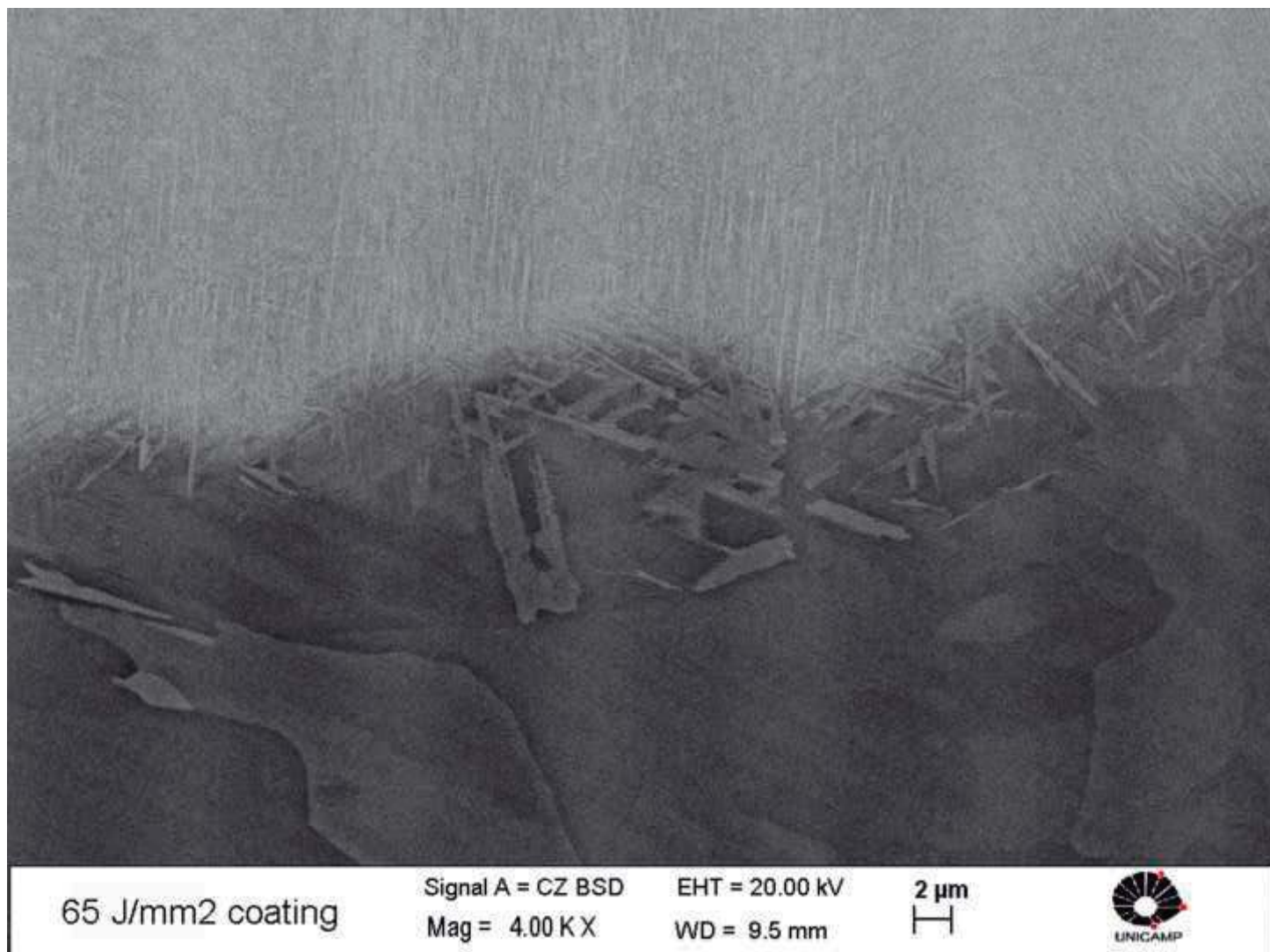


Figure 6a  
[Click here to download high resolution image](#)

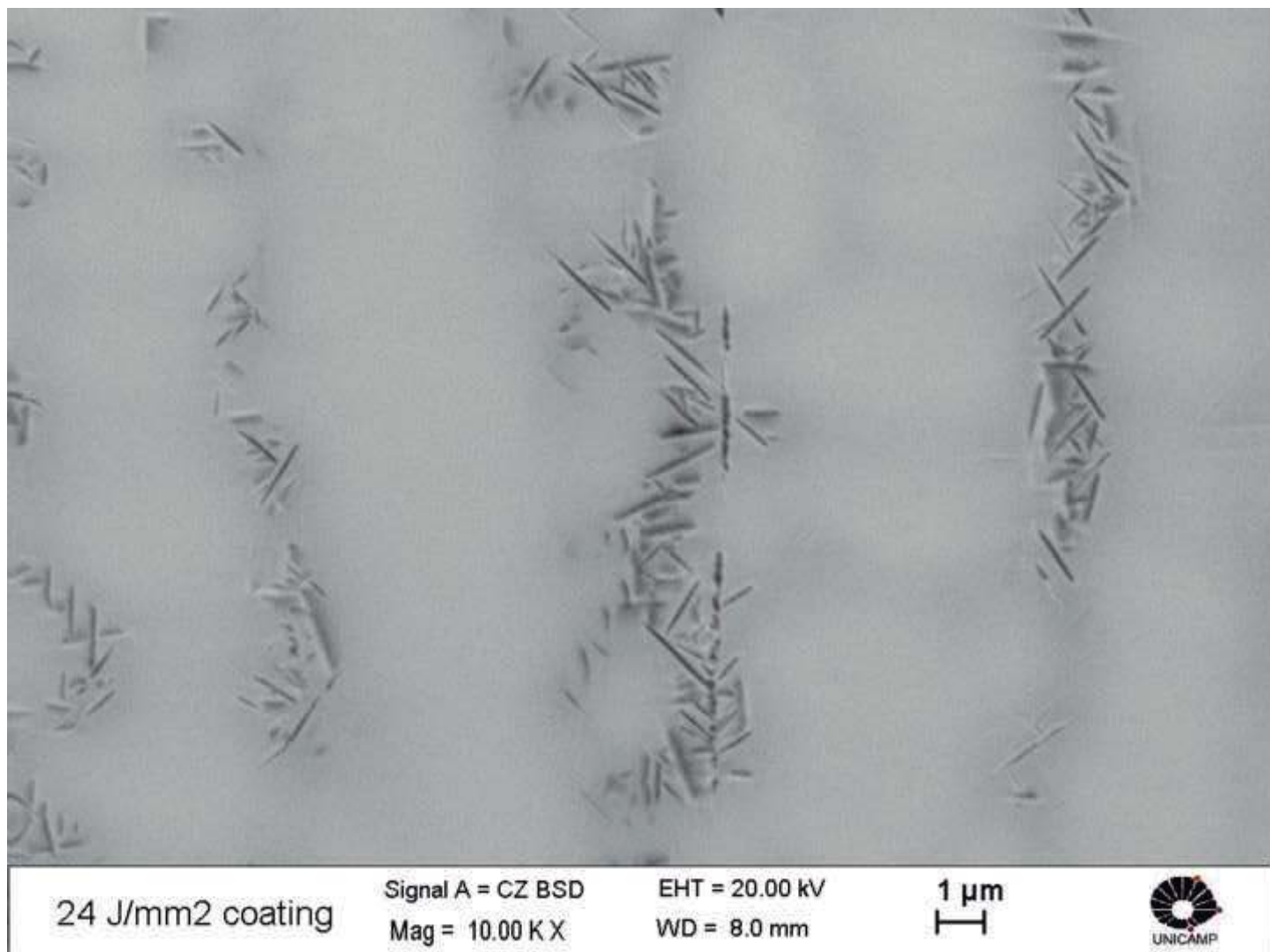


Figure 6b  
[Click here to download high resolution image](#)

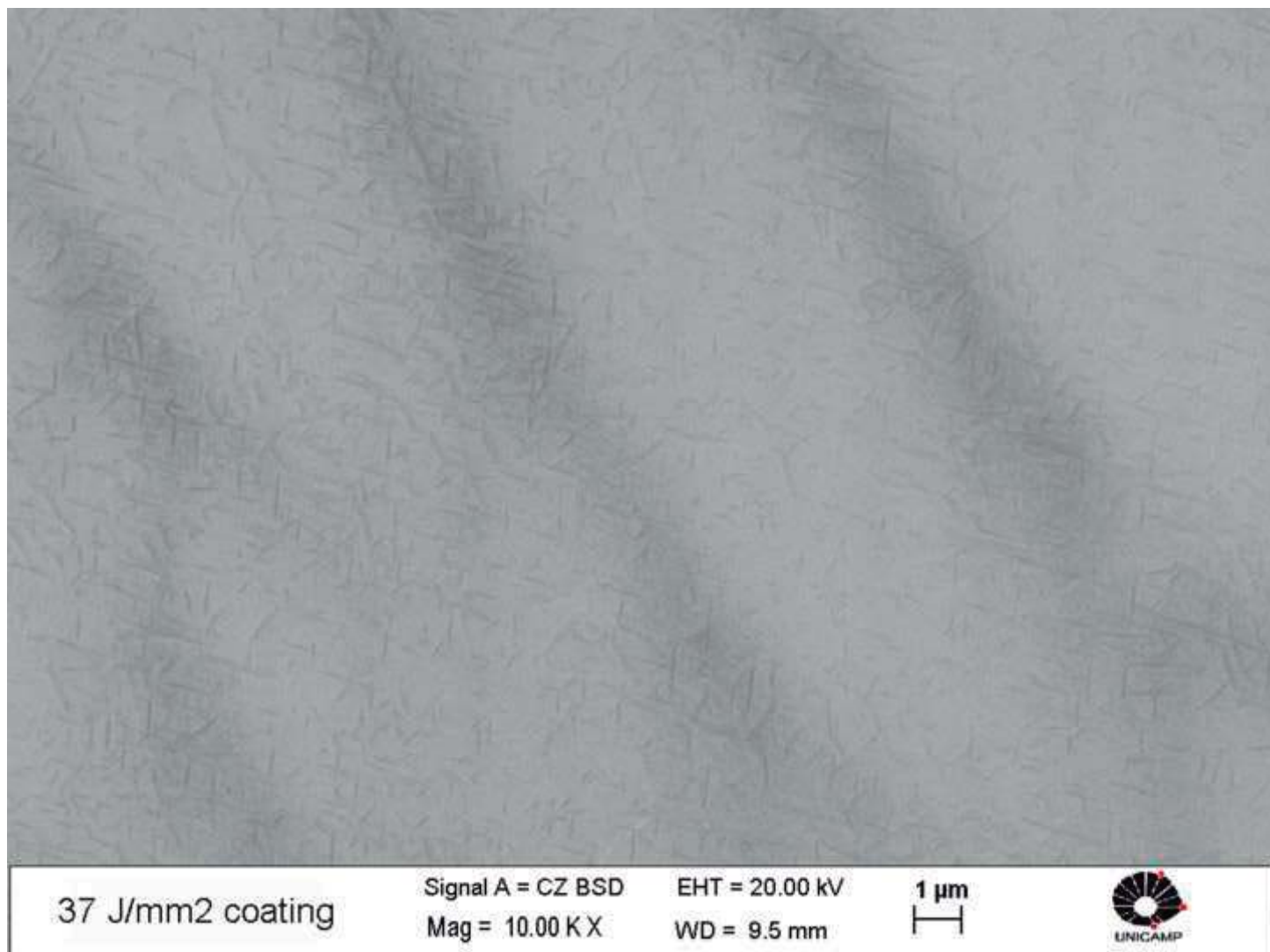


Figure 6c  
[Click here to download high resolution image](#)

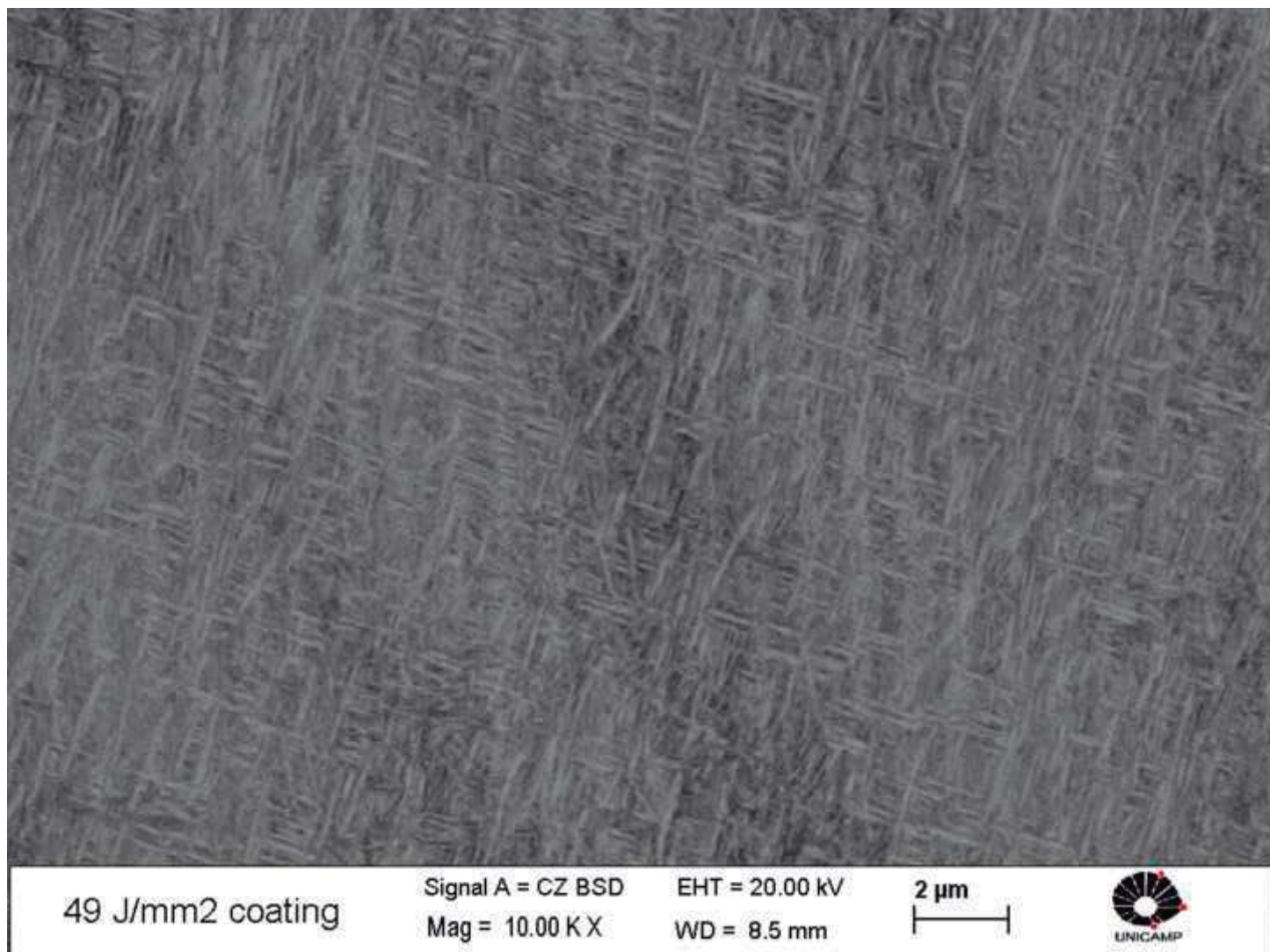


Figure 6d  
[Click here to download high resolution image](#)

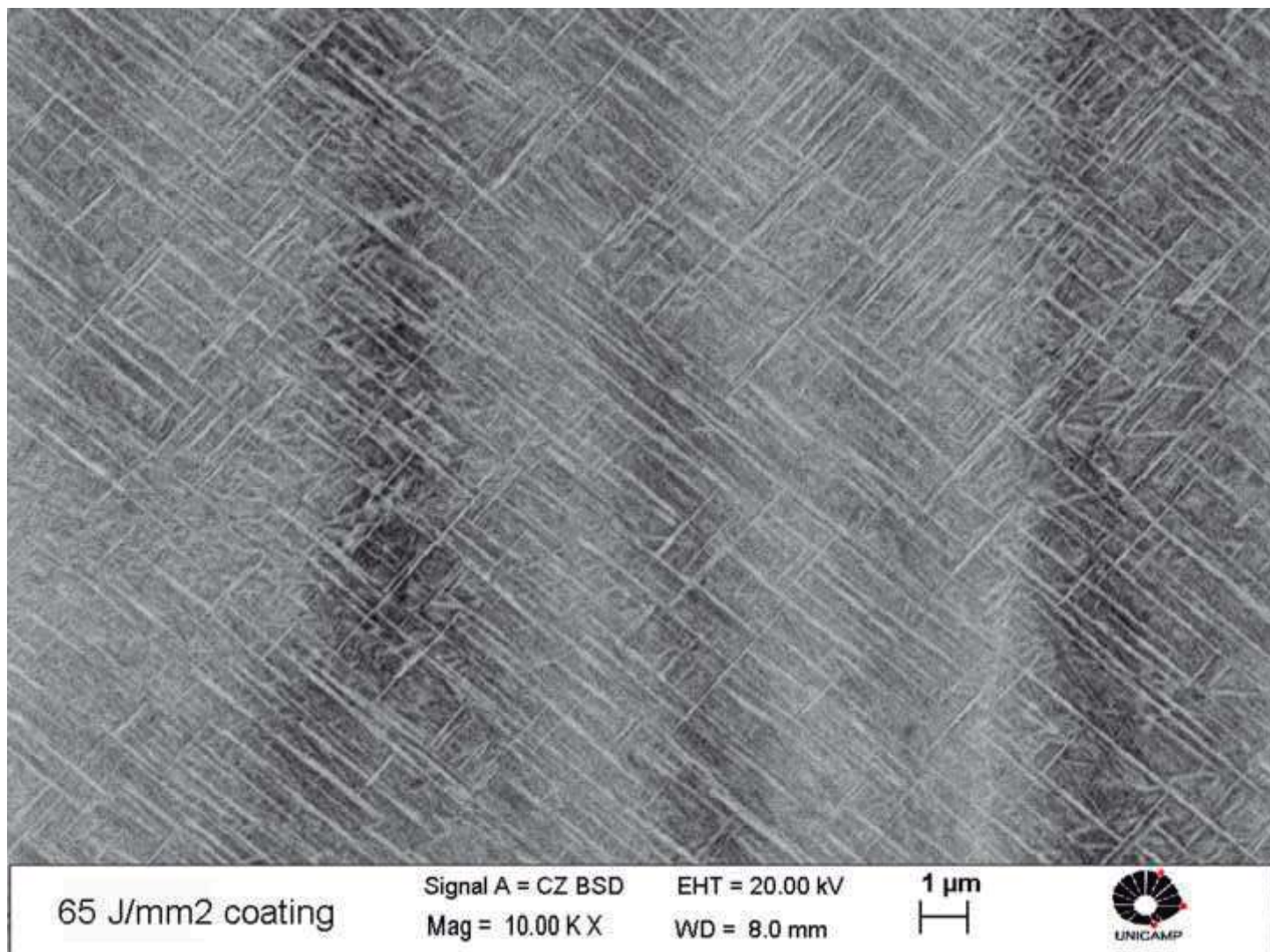


Figure 7  
[Click here to download high resolution image](#)

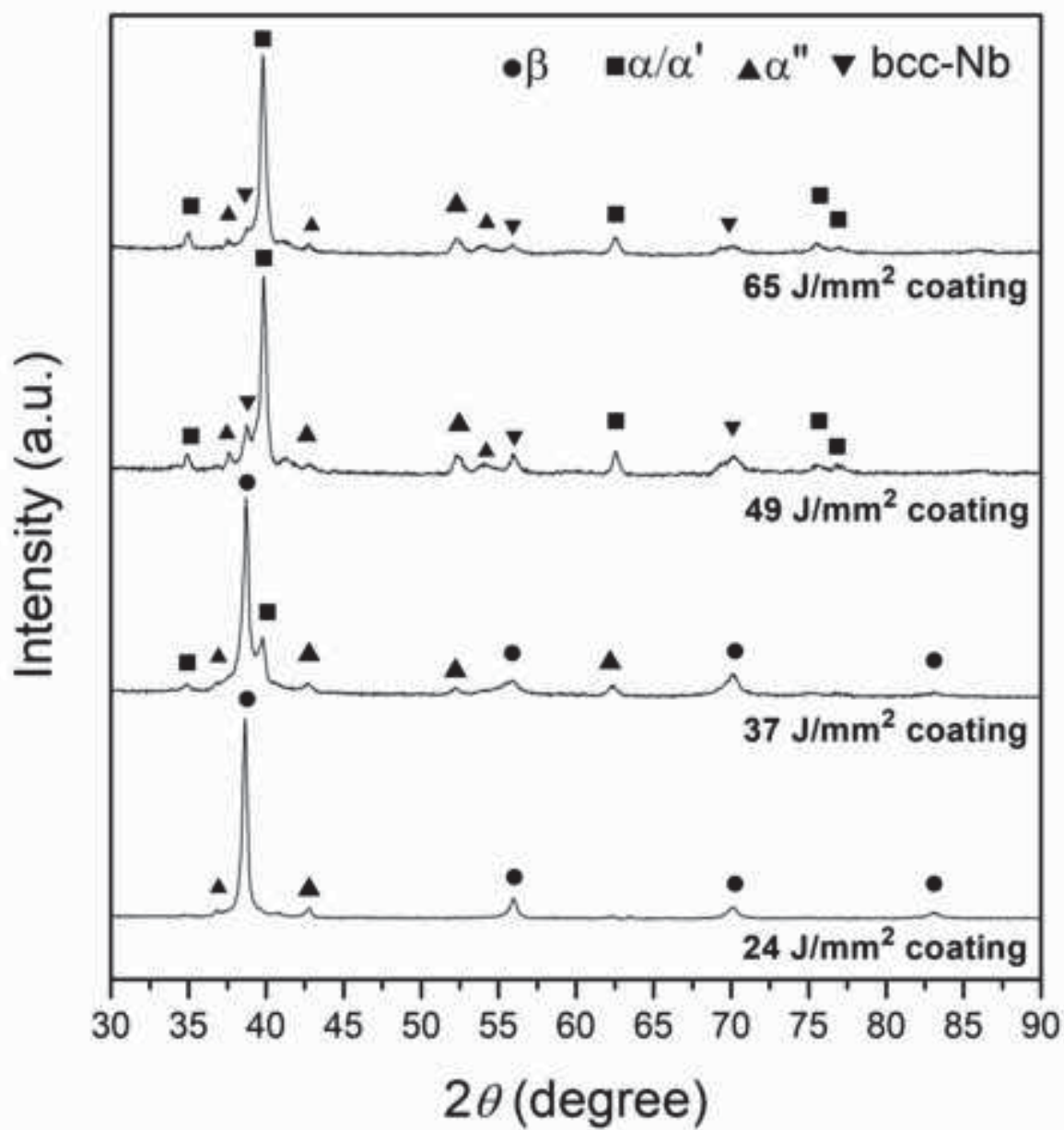


Figure 8  
[Click here to download high resolution image](#)

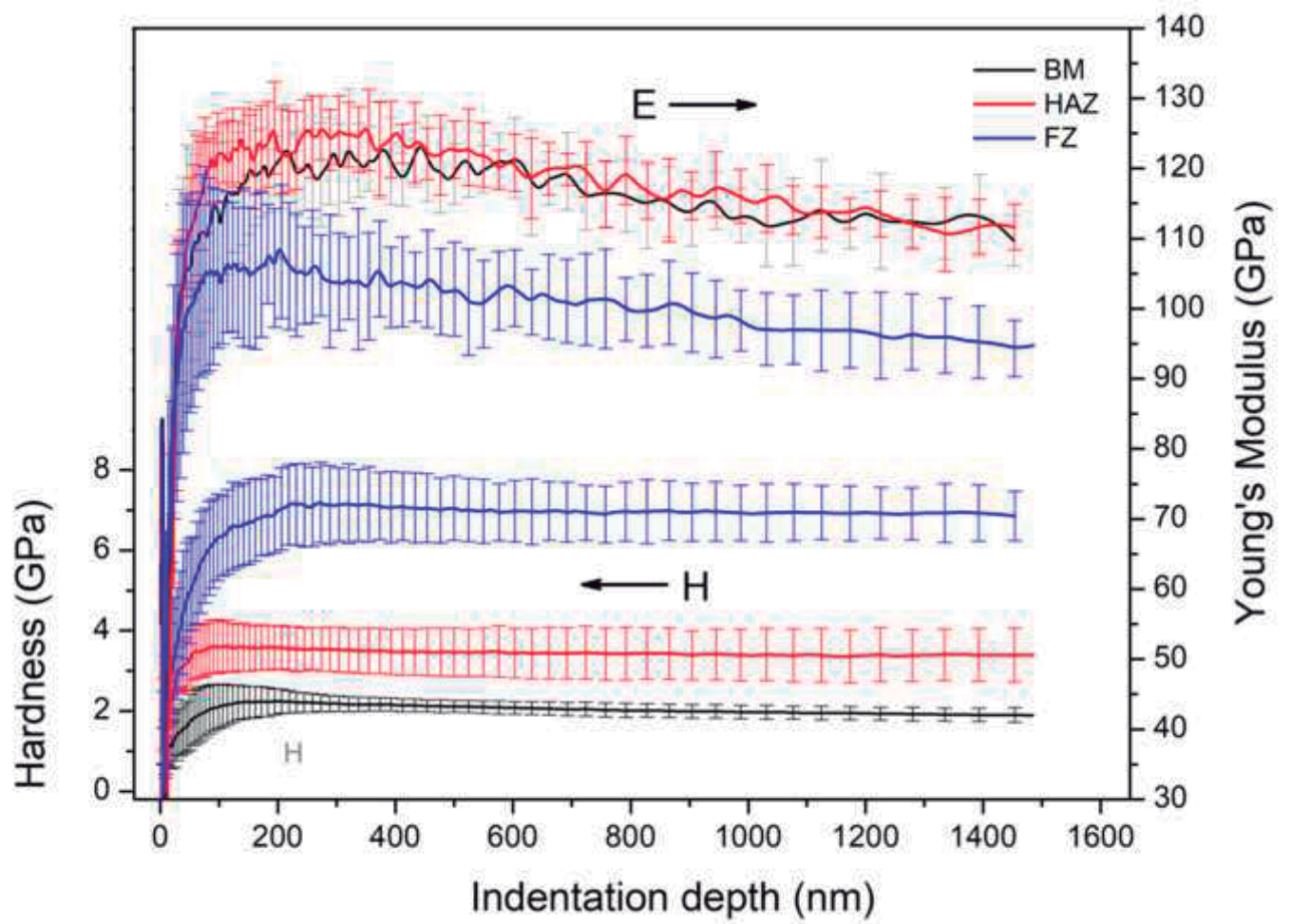


Figure 9  
[Click here to download high resolution image](#)

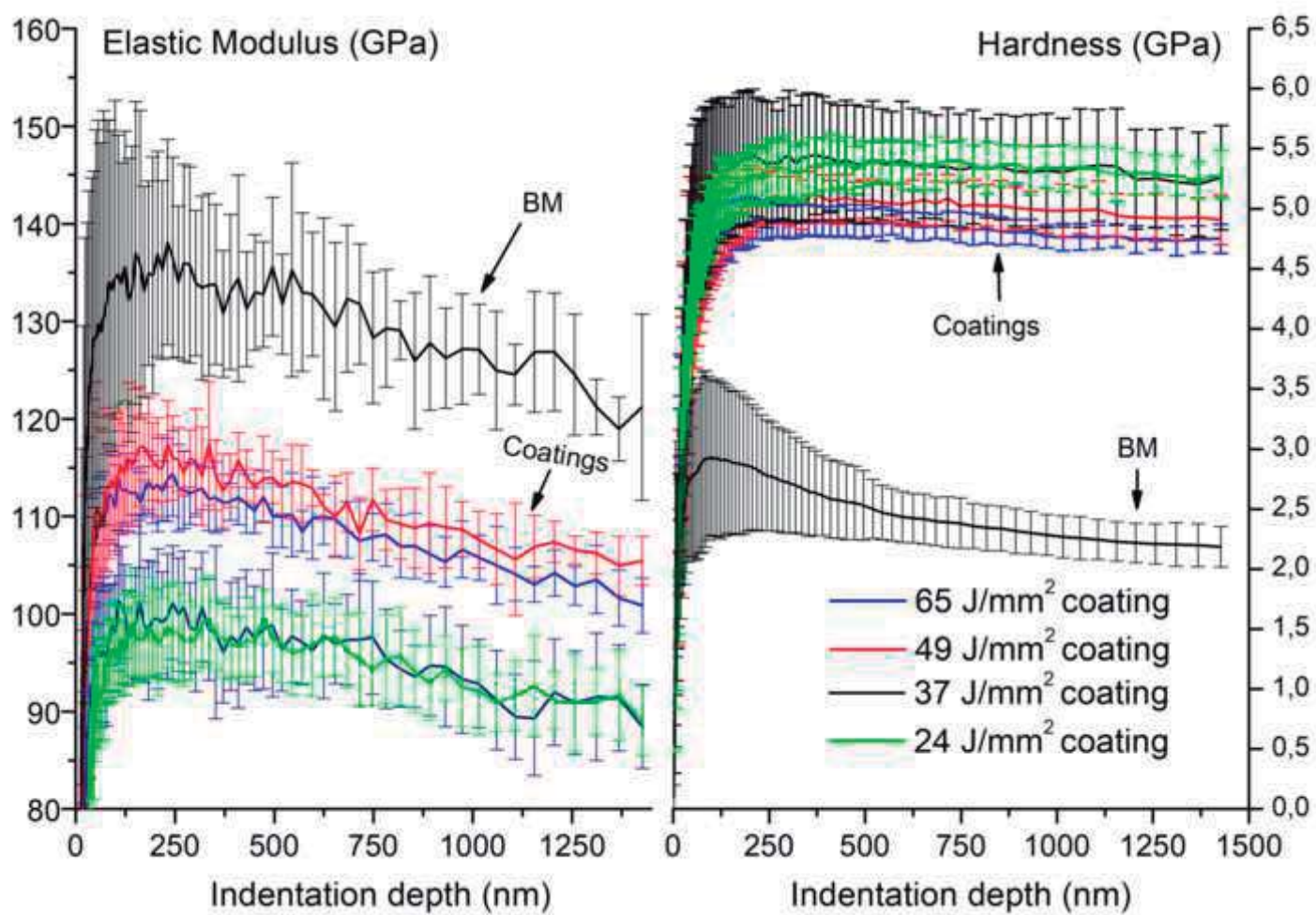
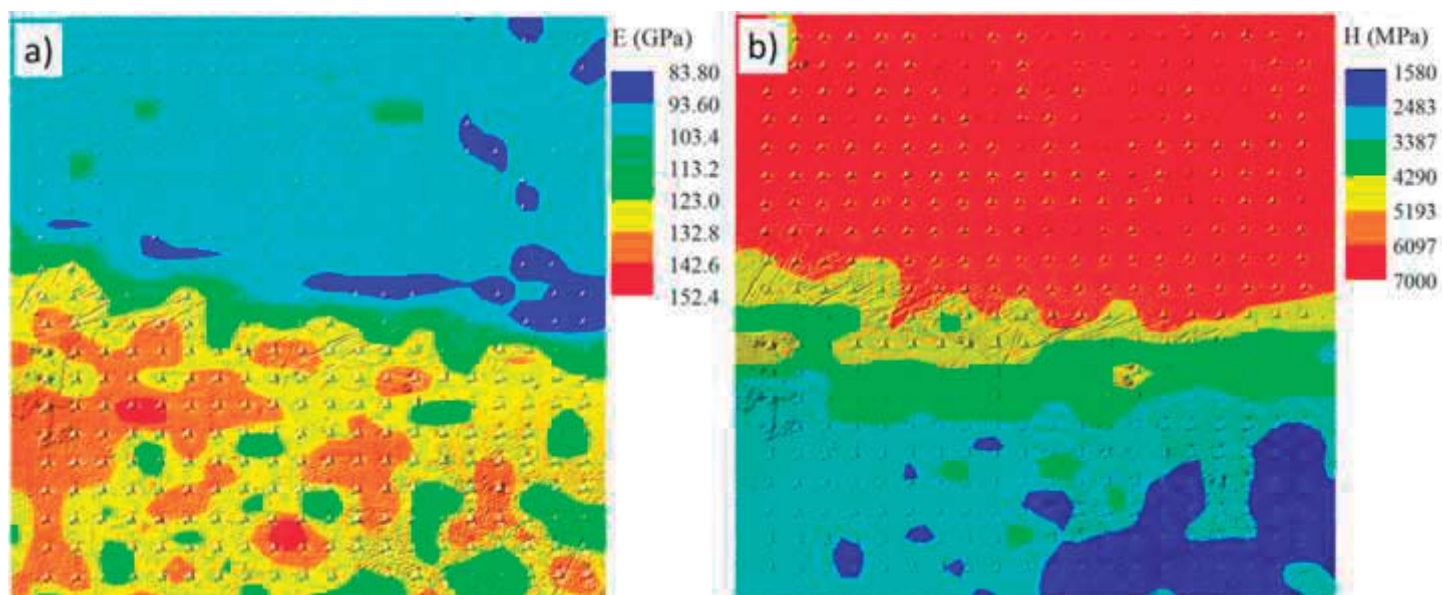


Figure 10  
[Click here to download high resolution image](#)



**\*Suggested Reviewers**

**Potential Reviewers**

Hamish Fraser, The Ohio State University, U.S.A..

[fraser.3@osu.edu](mailto:fraser.3@osu.edu)

Professor Hamish Fraser has a strong knowledge about the physical metallurgy of titanium and its alloys.

Ma Qian, Royal Melbourne Institute of Technology, Australia.

[ma.qian@rmit.edu.au](mailto:ma.qian@rmit.edu.au)

Professor Ma Qian has a strong knowledge about processing and characterization of titanium and its alloys.

Elena Gordo, Universidad Carlos III de Madrid, Spain.

[egordo@ing.uc3m.es](mailto:egordo@ing.uc3m.es)

Dra. Elena Gordo has a strong knowledge about processing and characterization of titanium and its alloys.

**Supplementary Material**

[Click here to download Supplementary Material: Elsevier Language Certificate.pdf](#)